The Astrophysical Journal, 869:23 (21pp), 2018 December 10 https://doi.org/10.3847/1538-4357/aaebfe

The Pickup Ion-mediated Solar Wind

G. P. Zank[1,2], L. Adhikari[1], L.-L. Zhao[1], P. Mostafavi[2,3], E. J. Zirnstein[3], and D. J. McComas[3]
[1] Center for Space Plasma and Aeronomic Research (CSPAR), University of Alabama in Huntsville, Huntsville, AL 35805, USA
[2] Department of Space Science, University of Alabama in Huntsville, Huntsville, AL 35899, USA
[3] Department of Astrophysical Sciences, Princeton University, Princeton, NJ 08544, USA
Received 2018 September 10; revised 2018 October 22; accepted 2018 October 24; published 2018 December 7

Abstract

The New Horizons Solar Wind Around Pluto (NH SWAP) instrument has provided the first direct observations of interstellar H^+ and He^+ pickup ions (PUIs) at distances between ∼11.26 and 38 au in the solar wind. The observations demonstrate that the distant solar wind beyond the hydrogen ionization cavity is indeed mediated by PUIs. The creation of PUIs modifies the underlying low-frequency turbulence field responsible for their own scattering. The dissipation of these low-frequency fluctuations serves to heat the solar wind plasma, and accounts for the observed non-adiabatic solar wind temperature profile and a possible slow temperature increase beyond ∼30 au. We develop a very general theoretical model that incorporates PUIs, solar wind thermal plasma, the interplanetary magnetic field, and low-frequency turbulence to describe the evolution of the large-scale solar wind, PUIs, and turbulence from 1–84 au, the structure of the perpendicular heliospheric termination shock, and the transmission of turbulence into the inner heliosheath, extending the classical models of Holzer and Isenberg. A detailed comparison of the theoretical model solutions and observations derived from the *Voyager* 2 and NH SWAP data sets shows excellent agreement between the two for reasonable physical parameters.

Key words: ISM: atoms – local interstellar matter – solar wind – Sun: heliosphere

1. Introduction

The New Horizons Solar Wind Around Pluto (NH SWAP) instrument (McComas et al. 2008) measures the thermal solar wind plasma and additionally has provided the first direct observations of interstellar H^+ and He^+ pickup ions (PUIs) at distances between ∼11.26 and 38 au in the solar wind (McComas et al. 2017). This region is well distant of the hydrogen ionization cavity (contained roughly within ∼5–8 au), and so the observed PUI distribution, particularly that of pickup H^+, should have had sufficient time to evolve into a stable nearly isotropic distribution. Prior observations of PUIs by the *Ulysses* Solar Wind Ion Composition Spectrometer instrument (Gloeckler et al. 1992) identified numerous PUI species (H^+, He^+, N^+, O^+, Ne^+) (e.g., Gloeckler & Geiss 1998). These observations were made within the hydrogen ionization cavity, from about 1.4–5.4 au, and the distributions tended to be highly anisotropic in character (Gloeckler et al. 1995). This suggested that the PUI scattering mean free path (mfp) was possibly unusually long, the precise reason being somewhat unclear. It has been suggested that the nature of the underlying turbulence responsible for the scattering of PUIs, being a superposition of a majority quasi-2D and a minority slab component, might be responsible for the long mfps. However, the initial PUI distribution, as a ring-beam, is unstable to the excitation of Alfvénic modes (Lee & Ip 1987; Williams & Zank 1994; Zank 1999; Cannon et al. 2014a, 2014b; Aggarwal et al. 2016; Fisher et al. 2016; Smith et al. 2017; Hollick et al. 2018a, 2018b), and therefore modifies the underlying low-frequency turbulence field responsible for scattering PUIs. It transpires that the excitation of Alfvénic fluctuations in the distant solar wind is key to understanding the observed radial evolution of the variance in magnetic field fluctuations (Zank et al. 1996; Matthaeus et al. 1999; Smith et al. 2001; Breech et al. 2008; Isenberg et al. 2010; Oughton et al. 2011; Zank et al. 2012a; Adhikari et al. 2014, 2015; Wiengarten et al. 2016; Adhikari et al. 2017; Shiota et al. 2017; Zank et al. 2017). Equally importantly, the dissipation of these low-frequency fluctuations serves to heat the solar wind plasma, and accounts for the non-adiabatic solar wind temperature profile and a possible slow temperature increase beyond ∼30 au (Williams et al. 1995; Matthaeus et al. 1999; Smith et al. 2001; Breech et al. 2008; Oughton et al. 2011; Adhikari et al. 2015; Zank et al. 2017). The excitation of low-frequency turbulence in the outer heliosphere also has an effect on cosmic ray mfps (Zank et al. 1998; Florinski et al. 2003; Engelbrecht & Burger 2013; Chhiber et al. 2017; Engelbrecht 2017; Zhao et al. 2017, 2018).

Evidently, there is a close coupling of PUIs, thermal solar wind plasma, and the evolution of low-frequency turbulence throughout the solar wind. Early solar wind models that include PUIs created by the flow of interstellar neutral H into the heliosphere typically assumed instantaneous assimilation and equilibration of newly created PUIs with the solar wind plasma (Wallis 1971; Holzer 1972; Holzer & Leer 1973; Isenberg et al. 1985) i.e., the combined thermal solar wind and PUI plasma was treated as a single distribution, and the closure of the fluid system assumed essentially a total Maxwellian distribution. These models predicted a quite dramatic solar wind temperature increase with increasing heliocentric distance, which is of course not observed. Isenberg (1986) pointed out that the Coulomb collision timescale between suprathermal pickup protons and solar wind protons (and electrons) far exceeds the fluid advection time for a heliospheric supersonic flow of radial extent less than 100 au (i.e., the distance to the heliospheric termination shock—HTS). Consequently, there can be no equilibration of the thermal solar wind and pickup proton populations, and instead the total distribution will comprise a cold thermal solar wind core and a tenuous energetic pickup proton halo (Isenberg 1986; Zank et al. 1996; Zank 1999; Zank et al. 2014, 2010; Zank 2015; Burrows et al. 2010). As discussed by Isenberg (1986) and further elaborated by Zank et al. (2014; see also Zank 2016), a model of the supersonic

solar wind must incorporate as distinct plasma components the thermal solar wind and the suprathermal pickup protons.

In this work, we extend the classical models of Holzer (1972) and Isenberg (1986) by coupling a detailed model of turbulence transport and dissipation to a multi-fluid description of the solar wind plasma. This allows us to properly examine the feedback between solar wind plasma heating, the modified large-scale solar wind velocity due to the creation of PUIs, and the driving of turbulence by solar wind and interstellar PUI sources.

An important motivation for this work is that it allows for the testing of pickup proton-mediated solar wind models within ~40 au against a suite of NH SWAP plasma observations, including pickup proton plasma parameters. It also allows for the extrapolation of solar wind and thermal solar wind plasma parameters to the HTS based on SWAP observations between ~11.26 and 38 au (Randol et al. 2012, 2013; McComas et al. 2017). By extrapolating the SWAP plasma parameters to ~75–84 au, we can test models of the HTS (McComas et al. 2017) of the kind developed by Mostafavi et al. (2017b). Unfortunately NH does not possess a magnetic field instrument, which limits our ability to fully evaluate the turbulence transport models.

In Section 2, we present the basic model, including the turbulence transport equations, illustrating the complex mutual coupling of pickup protons, turbulence, and solar wind thermal plasma. Solutions for the supersonic solar wind models are presented in Section 3, and we compare to observations derived from *Voyager* 2 plasma and magnetometer data and NH SWAP plasma data. Section 3 includes extrapolation of the plasma and magnetic field model to ~84 au. This set of values is used in Section 4 to model the structure of the HTS based on a corresponding PUI-mediated plasma model. Finally, in Section 5, we use the turbulence model and the derived HTS shock structure results to consider the transmission of turbulence through the HTS into the inner heliosheath.

2. Model Equations

The derivation of the model equations on which we base the subsequent analysis, including the structure of the HTS, can be found in Zank et al. (2014; see also Zank 2016 for the correct form of the viscous stress tensor) and Zank et al. (2017). Based on the Zank et al. (2014) equations, Mostafavi et al. (2017b) discussed the structure of shocks in a pickup proton-mediated plasma, including an example of the HTS. Adhikari et al. (2017) solved the spherically symmetric form of the Zank et al. (2017) turbulence transport equations from 1–75 au for a prescribed constant radial solar wind speed.

In deriving the equations describing a non-equilibrated thermal plasma and a nearly isotropic suprathermal PUI distribution, Zank et al. (2014) assumed that pre-existing and self-generated Alfvén waves scatter PUIs. A form of collisionless Chapman–Enskog expansion then yields the appropriate form of the nearly isotropic PUI equations that describe the evolution of the PUI density ρ_p, velocity, and pressure P_p. Because of the near isotropy of the scattered PUI distribution, the fluid description for PUIs contains both a heat conduction term $\propto \boldsymbol{K}_p \cdot \nabla P_p$, where $\boldsymbol{K}_p$ is the collisionless PUI "thermal conduction" tensor, and a stress tensor due to the collisionless viscosity η_{ij}. The heat conduction term represents a first-order anisotropy and the viscous terms a second-order anisotropy in the PUI distribution. Although we neglect, for simplicity, the scale lengths introduced by both PUI heat conduction and viscosity in our model of the large-scale supersonic solar wind, they are of importance in determining the structure of the HTS, as will be discussed in Section 4.

In the low-frequency or magnetohydrodynamic (MHD)-like reduction of the full multi-fluid thermal plasma (thermal protons and electrons) and pickup proton gas, the tenuous pickup protons co-move with the dominant (by number) thermal plasma constituent (Zank et al. 2014). This yields after suitable approximation the MHD-like Equations (61)–(68) in Zank et al. (2014), in which both a distinct scalar thermal pressure P_s and pickup proton pressure P_p are present. These equations need to be modified by the effects of interstellar proton pickup due to photoionization of interstellar neutral H and both thermal proton and pickup proton charge exchange with interstellar neutral H traversing the heliosphere. The underlying basis of the derivation of the continuum model and source terms from a kinetic perspective is discussed in the Appendix. The thermal plasma (ρ_s) and pickup proton (ρ_p) density equations may be expressed separately as

$$\frac{\partial \rho_s}{\partial t} + \nabla \cdot (\rho_s \boldsymbol{U}) = -S_c^s; \tag{1}$$

$$\frac{\partial \rho_p}{\partial t} + \nabla \cdot (\rho_p \boldsymbol{U}) = S_c^s + S_p^{ph}, \tag{2}$$

where S_c^s denotes a charge-exchange source term and S_p^{ph} a photoionization source term, the specific forms of which are presented below, and $\boldsymbol{U}$ is the co-moving bulk flow velocity. Equations (1) and (2) can of course be combined in terms of the total density $\rho \equiv \rho_s + \rho_p$, i.e.,

$$\frac{\partial \rho}{\partial t} + \nabla \cdot (\rho \boldsymbol{U}) = S_p^{ph}. \tag{3}$$

The conservation form of the total momentum equation can be expressed as

$$\frac{\partial}{\partial t}(\rho \boldsymbol{U}) + \nabla \cdot \Big[\rho \boldsymbol{U}\boldsymbol{U} + P_s \boldsymbol{I} + P_p \boldsymbol{I} + \boldsymbol{\Pi}_p + \frac{1}{2\mu_0} B^2 \boldsymbol{I} - \frac{1}{\mu_0}\boldsymbol{B}\boldsymbol{B}\Big] = \boldsymbol{S}_p^m + \boldsymbol{U}_{\rm H} S_p^{ph}, \tag{4}$$

where Π_p is the pickup proton stress tensor,

$$\boldsymbol{\Pi}_p = \frac{\eta}{15}\begin{pmatrix} 1 - 3\cos^2\theta & 3\cos\theta\sin\theta & 0 \\ 3\cos\theta\sin\theta & 1 - 3\sin^2\theta & 0 \\ 0 & 0 & 1 \end{pmatrix} \times \left(b_k b_l \frac{\partial U_l}{\partial x_k} - \frac{1}{3}\frac{\partial U_m}{\partial x_m}\right). \tag{5}$$

Here, θ is the angle between the flow $\boldsymbol{U}$ and magnetic field $\boldsymbol{B}$ vectors, where $\boldsymbol{B}$ is along the $\boldsymbol{x}$-direction, $\boldsymbol{b} \equiv \boldsymbol{B}/|\boldsymbol{B}|$ is a directional unit vector, μ_0 the permeability of free space, and $\eta \sim P_p \tau_s / m_p$ is the collisionless pickup proton viscosity and can be approximated in a "classical" form that resembles the usual collisional viscosity (see Zank et al. 2014) (τ_s denotes a characteristic wave-particle scattering time and m_p the proton mass). Expression (5) can be expressed in the classical stress tensor form (Zank et al. 2014), not shown here. The PUI stress tensor was derived originally in a coordinate system in which the magnetic field $\boldsymbol{B}$ defined the "z-direction" (Zank et al. 2014;

Zank 2016). In rewriting the PUI stress tensor in the form of Equation (5), we introduced an arbitrary coordinate system in which θ is the angle between the flow vector and the magnetic field vector. This follows from a straightforward rotation of the coordinates so we do not provide the details (this is the same rotation that introduces the off-diagonal terms in the PUI heat flux tensor). Because we use the $\boldsymbol{x}$ direction to define the orientation of the magnetic field, when $\theta = 0$, the diagonal of the matrix becomes $(-2, 1, 1)$, but in Zank et al. (2014), the diagonal of their matrix in Equation (44) is $(1, 1, -2)$ since they used the z-axis to define the magnetic field direction. Both the PUI heat conduction and viscous terms are important in the context of the HTS structure problem (Mostafavi et al. 2017b) and are used in Section 4 below, but are not important for modeling the large-scale steady-state supersonic solar wind. Two source terms are present in (4), one being the momentum introduced by the photoionized PUIs, where $\boldsymbol{U}_{\rm H}$ is the interstellar neutral H velocity in the heliosphere, and the other due to the charge-exchange creation of PUIs. For the present, we do not include the possible contribution to the momentum budget by turbulence. This would require a Reynolds-averaged form of the equations, which has been discussed by Kryukov et al. (2012) and Usmanov et al. (2011, 2014). For a smooth flow, Equation (4) reduces to

$$\rho\left(\frac{\partial \boldsymbol{U}}{\partial t} + \boldsymbol{U}\cdot\nabla\boldsymbol{U}\right) + \nabla P_s + \nabla P_p - \boldsymbol{J}\times\boldsymbol{B} + \nabla\cdot\boldsymbol{\Pi}_p = \boldsymbol{S}_p^m + (\boldsymbol{U}_{\rm H} - \boldsymbol{U})S_p^{ph}, \quad (6)$$

where the current is as usual given by $\mu_0\boldsymbol{J} = \nabla\times\boldsymbol{B}$.

The total energy equation includes the heat flux associated with the nearly isotropic pickup protons. Furthermore, the dissipation of turbulence leads to heating of the plasma. Both these factors yield the total energy equation and the pickup proton pressure equation in the form (Zank et al. 2014; Zank 2016)

$$\frac{\partial}{\partial t}\left(\frac{1}{2}\rho U^2 + \frac{P_s}{\gamma_s - 1} + \frac{P_p}{\gamma_p - 1} + \frac{B^2}{2\mu_0}\right) + \nabla\cdot\left[\frac{1}{2}\rho U^2\boldsymbol{U} + \frac{\gamma_s}{\gamma_s - 1}P_s\boldsymbol{U} + \frac{\gamma_p}{\gamma_p - 1}P_p\boldsymbol{U} + \frac{B^2}{\mu_0}\boldsymbol{U} + \boldsymbol{\Pi}_p\cdot\boldsymbol{U} - \frac{1}{\mu_0}\boldsymbol{U}\cdot\boldsymbol{B}\boldsymbol{B} - \frac{1}{\gamma_p - 1}\frac{1}{3}\boldsymbol{K}_p\cdot\nabla P_p\right] = S_p^e + S_t; \quad (7)$$

$$\frac{\partial P_p}{\partial t} + \boldsymbol{U}\cdot\nabla P_p + \gamma_p P_p\nabla\cdot\boldsymbol{U} = \frac{1}{3}\nabla\cdot(\boldsymbol{K}_p\cdot\nabla P_p) - (\gamma_p - 1)\boldsymbol{\Pi}_p : (\nabla\boldsymbol{U}) + (\gamma_p - 1)S_p^e, \quad (8)$$

where S_p^e denotes a pickup proton energy source term due to charge exchange and S_t a source of heating due to the dissipation of turbulence. The thermal plasma and pickup proton adiabatic indices are given by $\gamma_{s,p}$, respectively, and we assume that both values are $5/3$ (although see Khabibrakhmanov et al. 1996; Zank 1999 for the possibility that γ_p could be different from $5/3$). Notice from Equation (8) that we have assumed explicitly that the dissipation of turbulence heats only the thermal plasma and not the suprathermal pickup protons. For smooth flows, the conservation form of Equation (7) can be re-expressed in terms of the thermal gas pressure, as is done below when the explicit source terms are included.

We restrict our attention to a simple 1D spherically symmetric steady-state solar wind and consider the source terms. The photoionization term can be expressed as (Holzer 1972; Isenberg 1986)

$$S_p^{ph} = \nu_{p0} m_p N\left(\frac{r_0}{r}\right)^2, \quad (9)$$

where N is the neutral H number density, $r_0 = 1$ au, and the ionization rate $\nu_{p0} = 1.5\times10^{-7}$ s^{-1}. Here,

$$N(r) = n_{\rm H}^{\infty}\exp\left(-\frac{L\theta'}{r\sin\theta'}\right), \quad (10)$$

where θ' is the angle between observation point and upstream direction. We use $\theta' = 0$, a hydrogen ionization cavity length scale $L = 7$ au, and $n_{\rm H}^{\infty} = 0.1$ cm^{-3}. The charge-exchange terms correspond to charge exchange between solar wind protons and interstellar neutral H (S_c^s) and between pickup protons and neutral H (S_c^p), given by (Isenberg 1986)

$$S_c^s = \nu_c^s\rho_s; \quad S_c^p = \nu_c^p\rho_p; \quad (11)$$

$$\nu_c^s \equiv \nu_{c0}N\left[\frac{128k}{9\pi m_p}(T_s + T_{\rm H}) + (\boldsymbol{U} - \boldsymbol{U}_{\rm H})^2\right]^{1/2}; \quad (12)$$

$$\nu_c^p \equiv \nu_{c0}N\left[\frac{128k}{9\pi m_p}(T_p + T_{\rm H}) + (\boldsymbol{U} - \boldsymbol{U}_{\rm H})^2\right]^{1/2}, \quad (13)$$

where $\nu_{c0} = 2\times10^{-15}$ cm^2 is the charge-exchange cross-section (Holzer 1972), k is Boltzmann's constant, and $T_{s/p}$ the thermal/pickup proton temperature. Note that ν_{p0} does not appear explicitly in the Vasyliunas & Siscoe (1976) distribution function since the assumption of (i) a cold neutral H distribution, (ii) a neutral H drift speed $U_{\rm H} = 0$, (iii) cold solar wind plasma, i.e., $T_s = 0$, a parameter β_0 that scales as r^{-2}, where r refers to heliocentric distance, yields a source term similar to the photoionization source term (9). Under these assumptions, the source term is effectively Equation (9) but with a multiplicative parameter β_0 that corresponds to Equation (1) of McComas et al. (2017). This point is discussed further in the Conclusions.

The stationary spherically symmetric continuity and momentum Equations (1)–(3) and (6) assume the form

$$\frac{1}{r^2}\frac{d}{dr}(r^2\rho U) = S_p^{ph} = \nu_{p0}m_p N\left(\frac{r_0}{r}\right)^2; \quad (14)$$

$$\frac{1}{r^2}\frac{d}{dr}(r^2\rho_s U) = -\nu_c^s\rho_s; \quad (15)$$

$$\frac{1}{r^2}\frac{d}{dr}(r^2\rho_p U) = \nu_c^s\rho_s + \nu_{p0}m_p N\left(\frac{r_0}{r}\right)^2; \quad (16)$$

$$\rho U\frac{dU}{dr} + \frac{dP_s}{dr} + \frac{dP_p}{dr} + (\nabla\cdot\boldsymbol{\Pi}_p)_r + \frac{B}{\mu_0}\frac{dB}{dr} = S_p^{ph}(U_{\rm H} - U) + (\nu_c^s\rho_s + \nu_c^p\rho_p)(U_{\rm H} - U), \quad (17)$$

where $(\nabla \cdot \mathbf{\Pi}_p)_r$ denotes the radial component of the vector $\nabla \cdot \mathbf{\Pi}_p$. The total energy equation requires a little more attention and the stationary spherically symmetric form of (7) is, after suitable rearrangement and assuming a smooth flow, given by

$$\begin{aligned}
&\frac{1}{\gamma_s - 1} U \frac{dP_s}{dr} + \frac{\gamma_s}{\gamma_s - 1} P_s \frac{1}{r^2}\frac{d}{dr}(r^2 U) \\
&+ \frac{1}{\gamma_p - 1} U \frac{dP_p}{dr} + \frac{\gamma_p}{\gamma_p - 1} P_p \frac{1}{r^2}\frac{d}{dr}(r^2 U) \\
&+ \Pi_{p_{rr}} \frac{\partial U}{\partial r} - \frac{1}{\gamma_p - 1}\frac{1}{3r^2}\frac{d}{dr}\left(r^2 K_{rr}\frac{dP_p}{dr}\right) \\
&= S_p^{ph}\left(\frac{1}{2}(U_{\rm H} - U)^2 + \frac{3}{2}\frac{kT_{\rm H}}{m_p}\right) \\
&+ \nu_c^s \rho_s \left(\frac{1}{2}(U_{\rm H} - U)^2 + \frac{3}{2}\frac{kT_{\rm H}}{m_p} - \frac{1}{\gamma_s - 1}\frac{kT_s}{m_p}\right) \\
&+ \nu_c^p \rho_p \left(\frac{1}{2}(U_{\rm H} - U)^2 + \frac{3}{2}\frac{kT_{\rm H}}{m_p} - \frac{1}{\gamma_p - 1}\frac{kT_p}{m_p}\right) + S_t, \quad (18)
\end{aligned}$$

and $\Pi_{p_{rr}}$ and K_{rr} denote the radial component of the viscous and stress tensors, respectively. On assuming that thermal protons lose energy due to charge exchange with interstellar H and that heating by turbulence occurs only for the thermal gas, we can separate the thermal gas pressure terms to obtain the stationary spherically symmetric thermal pressure equation,

$$U\frac{dP_s}{dr} + \gamma_s P_s \frac{1}{r^2}\frac{d}{dr}(r^2 U) = -\nu_c^s \rho_s \frac{kT_s}{m_p} + (\gamma_s - 1) S_t. \quad (19)$$

Similarly, the pickup proton pressure equation is given by

$$\begin{aligned}
&U\frac{dP_p}{dr} + \gamma_p P_p \frac{1}{r^2}\frac{d}{dr}(r^2 U) = \frac{1}{3r^2} \\
&\times \frac{d}{dr}\left(r^2 K_{rr}\frac{dP_p}{dr}\right) - (\gamma_p - 1)\Pi_{p_{rr}}\frac{\partial U}{\partial r} \\
&+ (\gamma_p - 1)(S_p^{ph} + \nu_c^s \rho_s + \nu_c^p \rho_p) \\
&\times \left(\frac{1}{2}(U_{\rm H} - U)^2 + \frac{3}{2}\frac{kT_{\rm H}}{m_p}\right) - \nu_c^p \rho_p \frac{kT_p}{m_p}. \quad (20)
\end{aligned}$$

For the large-scale or mean magnetic field, we assume an azimuthal field only, governed by

$$\frac{1}{r}\frac{d}{dr}(rUB) = 0; \quad \text{i.e.,} \quad \frac{B(r)}{B_0} = \frac{r_0}{r}\left(\frac{U}{U_0}\right)^{-1}, \quad (21)$$

where $U_0 = U(1\ \text{au})$ and $B_0 = B(1\ \text{au})$.

To evaluate the turbulence heating term S_t, we need to describe the transport and dissipation of turbulence throughout the heliosphere, ensuring that the appropriate sources of turbulence are identified as well as that associated with pickup ion creation in the distant solar wind. The turbulence transport model we use is that of Zank et al. (2017). The current paradigm for fully developed turbulence in the solar wind is that it is a superposition of a majority quasi-2D component and a minority slab component, e.g., Matthaeus et al. (1995). The nearly incompressible (NI) reduction of MHD in the plasma beta $\beta_p \sim 1$ regime, appropriate to most of the solar wind, shows that such a decomposition (quasi-2D plus slab) arises naturally in the presence of a sufficiently strong guide magnetic field (Zank & Matthaeus 1992, 1993; Hunana & Zank 2010). The stationary form of the NI MHD transport equations describing the evolution of the majority quasi-2D component in a spherically symmetric solar wind with an azimuthal magnetic field can be expressed as (Adhikari et al. 2017; Zank et al. 2017)

$$\begin{aligned}
&U\frac{d}{dr}\langle z^{\infty\pm 2}\rangle + \frac{1}{2}\left(\frac{2U}{r} + \frac{dU}{dr}\right)\langle z^{\infty\pm 2}\rangle \\
&+ \frac{1}{2}\left(\frac{2U}{r} + \frac{dU}{dr}\right)E_D^{\infty} \\
&- \frac{1}{2}\langle z^{\infty\pm 2}\rangle^{1/2}(\langle z^{\infty\pm 2}\rangle - E_D^{\infty})\frac{1}{\rho_s}\frac{d\rho_s}{dr} \\
&= -2\frac{\langle z^{\infty\pm 2}\rangle \langle z^{\infty\mp 2}\rangle^{1/2}}{\lambda_{\infty}^{\pm}} + 2\frac{\langle z^{*\pm 2}\rangle \langle z^{*\mp 2}\rangle^{1/2}}{\lambda^{*\pm}} \\
&+ 2C_{\rm sh}^{\pm}\frac{r_0|\Delta U|V_A^2}{r^2}; \quad (22)
\end{aligned}$$

$$\begin{aligned}
&U\frac{dE_D^{\infty}}{dr} + \frac{1}{2}\left(\frac{2U}{r} + \frac{dU}{dr}\right)E_D^{\infty} \\
&+ \frac{1}{2}E_T^{\infty}\left(\frac{2U}{r} + \frac{dU}{dr}\right) \\
&- \frac{1}{4}(E_D^{\infty} - \langle z^{\infty+2}\rangle^{1/2}\langle z^{\infty-2}\rangle^{1/2}) \\
&\times (\langle z^{\infty+2}\rangle^{1/2} + \langle z^{\infty-2}\rangle^{1/2})\frac{1}{\rho_s}\frac{d\rho_s}{dr} \\
&= -E_D^{\infty}\left(\frac{\langle z^{\infty-2}\rangle^{1/2}}{\lambda_{\infty}^{+}} + \frac{\langle z^{\infty+2}\rangle^{1/2}}{\lambda_{\infty}^{-}}\right) \\
&+ E_D^{*}\left(\frac{\langle z^{*-2}\rangle^{1/2}}{\lambda^{*+}} + \frac{\langle z^{*+2}\rangle^{1/2}}{\lambda^{*-}}\right) \\
&+ 2C_{\rm sh}^{E_D}\frac{r_0|\Delta U|V_A^2}{r^2}; \quad (23)
\end{aligned}$$

$$\begin{aligned}
&U\frac{dL_{\infty}^{\pm}}{dr} + \frac{1}{2}\left(\frac{2U}{r} + \frac{dU}{dr}\right)L_{\infty}^{\pm} \\
&+ \frac{1}{4}\left(\frac{2U}{r} + \frac{dU}{dr}\right)L_D^{\infty} \\
&+ \frac{1}{4}\langle z^{\infty\pm 2}\rangle^{1/2}(L_D^{\infty} - 2L_{\infty}^{\pm})\frac{1}{\rho_s}\frac{d\rho_s}{dr} = 0; \quad (24)
\end{aligned}$$

$$\begin{aligned}
&U\frac{dL_D^{\infty}}{dr} + \frac{1}{2}\left(\frac{2U}{r} + \frac{dU}{dr}\right)L_D^{\infty} \\
&+ \frac{1}{2}\left(\frac{2U}{r} + \frac{dU}{dr}\right)(L_{\infty}^{+} + L_{\infty}^{-}) \\
&- \frac{1}{4}(L_D^{\infty}(\langle z^{\infty+2}\rangle^{1/2} + \langle z^{\infty-2}\rangle^{1/2}) - 2L_{\infty}^{+}\langle z^{\infty-2}\rangle^{1/2} \\
&- 2L_{\infty}^{-}\langle z^{\infty+2}\rangle^{1/2})\frac{1}{\rho_s}\frac{d\rho_s}{dr} = 0. \quad (25)
\end{aligned}$$

Here, $z^{\infty\pm} \equiv \boldsymbol{u}^{\infty} \pm \boldsymbol{B}^{\infty}/\sqrt{\mu_0 \rho_s}$ are the forward and backward Elsässer variables, combining the quasi-2D fluctuating velocity field $\boldsymbol{u}^{\infty}$ and the fluctuating magnetic field $\boldsymbol{B}^{\infty}$ through the fluctuating (turbulent) Alfvén velocity $\boldsymbol{B}^{\infty}/\sqrt{\mu_0 \rho_s}$. The

variance of the fluctuating Elsässer variables is denoted by $\langle z^{\infty\pm 2}\rangle$, where the operator $\langle\cdot\rangle$ averages over small scales and high frequencies. The quasi-2D residual energy (or energy difference) is defined by $E_D^{\infty} \equiv \langle \boldsymbol{z}^{\infty +}\cdot \boldsymbol{z}^{\infty -}\rangle = \langle u^{\infty 2}\rangle - \langle B^{\infty 2}\rangle/(\mu_0\rho_s)$. The total fluctuating quasi-2D energy is denoted by $E_T^{\infty} \equiv (\langle z^{\infty +2}\rangle + \langle z^{\infty -2}\rangle)/2$, and the quasi-2D correlation lengths $\lambda_{\infty}^{\pm}$ are related to the correlation functions $L_{\infty}^{\pm}$ through $L_{\infty}^{\pm} = \langle z^{\infty\pm 2}\rangle \lambda_{\infty}^{\pm}$. Finally, L_D^{∞} is a correlation function related to the residual energy. The energy for the forward and backward slab Elsässer variables $\langle z^{*\pm 2}\rangle$ and the slab correlation length $\lambda^{*\pm}$ are discussed further below. However, we note that the quasi-2D and slab components are coupled, capturing the 3-mode coupling (Shebalin et al. 1983; Zank et al. 2017) that governs spectral transfer in the inertial range. This is expressed by the source-like terms in Equations (22) and (23) that contain the slab variables. Equations (22) and (23) contain genuine source terms associated with stream shear (Adhikari et al. 2017; Zank et al. 2017), where $C_{\rm sh}^{\pm}$ denotes the strength of the stream-shear source of forward or backward quasi-2D fluctuations, $|\Delta U|$ the characteristic velocity jump across the stream, and $V_{\rm A}$ the large-scale Alfvén speed. A lengthy derivation and discussion of these equations can be found in Zank et al. (2017) and specific solutions appropriate to a prescribed large-scale solar wind can be found in Adhikari et al. (2017).

The minority slab component steady-state spherically symmetric equations take the form (Adhikari et al. 2017; Zank et al. 2017)

$$
\begin{aligned}
&U\frac{d\langle z^{*\pm 2}\rangle}{dr} - (2b-1)\left(\frac{U}{r}+\frac{1}{2}\frac{dU}{dr}\right)\\
&\times\langle z^{*\pm 2}\rangle + \left(3b-\frac{1}{2}\right)\left(\frac{2U}{r}+\frac{dU}{dr}\right)E_D^{*}\\
&-\frac{1}{2}\left(\langle z^{*\pm 2}\rangle - E_D^{*}\right)\frac{\langle z^{\infty\pm 2}\rangle^{1/2}}{\rho_s}\frac{d\rho_s}{dr}\\
&= -2\frac{\langle z^{*\pm 2}\rangle\langle z^{\infty\mp 2}\rangle^{1/2}}{\lambda_{\infty}^{\pm}} - 2\frac{\langle z^{*\pm 2}\rangle\langle z^{*\mp 2}\rangle^{1/2}}{\lambda_{*}^{\pm}}\\
&+ 2C^{*}{}_{\rm sh}^{\pm}\frac{r_0|\Delta U|V_A^2}{r^2} + \frac{f_D n_{\rm H}^{\infty} U V_A}{n_{SW}^0\tau_{\rm ion}^0}\exp\left(\frac{-L}{r}\right);
\end{aligned}
\tag{26}
$$

$$
\begin{aligned}
&U\frac{dE_D^{*}}{dr} - (2b-1)\left(\frac{U}{r}+\frac{1}{2}\frac{dU}{dr}\right)E_D^{*}\\
&+\left(3b-\frac{1}{2}\right)\left(\frac{2U}{r}+\frac{dU}{dr}\right)E_T^{*}\\
&-\frac{1}{4}\Bigg(E_D^{*}\left(\langle z^{\infty +2}\rangle^{1/2}+\langle z^{\infty -2}\rangle^{1/2}\right) - \langle z^{*-2}\rangle\\
&\times\langle z^{\infty +2}\rangle^{1/2} - \langle z^{*+2}\rangle\langle z^{\infty -2}\rangle^{1/2}\Bigg)\frac{1}{\rho_s}\frac{d\rho_s}{dr}\\
&= -E_D^{*}\left(\frac{\langle z^{\infty -2}\rangle^{1/2}}{\lambda_{\infty}^{+}}+\frac{\langle z^{\infty +2}\rangle^{1/2}}{\lambda_{\infty}^{-}}\right) - E_D^{*}\\
&\times\left(\frac{\langle z^{*-2}\rangle^{1/2}}{\lambda_{*}^{+}}+\frac{\langle z^{*+2}\rangle^{1/2}}{\lambda_{*}^{-}}\right) + 2C^{*}{}_{\rm sh}^{E_D}\frac{r_0|\Delta U|V_A^2}{r^2};
\end{aligned}
\tag{27}
$$

$$
\begin{aligned}
&U\frac{dL_{*}^{\pm}}{dr} - (2b-1)\left(\frac{U}{r}+\frac{1}{2}\frac{dU}{dr}\right)L_{*}^{\pm}\\
&+\left(2b-\frac{1}{4}\right)\frac{U}{r}L_D^{*} + \frac{1}{2}\left(3b-\frac{1}{2}\right)\frac{dU}{dr}L_D^{*}\\
&-\frac{1}{2}\left(L_{*}^{\pm}-\frac{1}{2}L_D^{*}\right)\langle z^{\infty\pm 2}\rangle^{1/2}\frac{1}{\rho_s}\frac{d\rho_s}{dr} = 0;
\end{aligned}
\tag{28}
$$

$$
\begin{aligned}
&U\frac{dL_D^{*}}{dr} - (2b-1)\left(\frac{U}{r}+\frac{1}{2}\frac{dU}{dr}\right)L_D^{*}\\
&+\left(3b-\frac{1}{2}\right)\left(\frac{2U}{r}+\frac{dU}{dr}\right)(L_{*}^{+}+L_{*}^{-})\\
&+\frac{1}{2}\Bigg[\left(L_{*}^{-}-\frac{1}{2}L_D^{*}\right)\langle z^{\infty +2}\rangle^{1/2} + \left(L_{*}^{+}-\frac{1}{2}L_D^{*}\right)\\
&\times\langle z^{\infty -2}\rangle^{1/2}\Bigg]\frac{1}{\rho_s}\frac{d\rho_s}{dr} = 0,
\end{aligned}
\tag{29}
$$

where the starred quantities are the slab turbulence versions of the "∞" quantities of quasi-2D turbulence. Were it not for the assumption of an azimuthal magnetic field, the large-scale background Alfvén velocity would typically enter the slab turbulence equations explicitly, introducing singular behavior when $U = V_A$ (Zank et al. 2012a, 2017, 2018; Adhikari et al. 2015, 2017). A structural similarity parameter b associated with the Alfvén velocity is present (Zank et al. 2012a). Note that the slab equations for the forward and backward Elsässer energy densities (26) contain a source term corresponding to the excitation of turbulence by the creation of PUIs (Zank et al. 2017). The residual energy Equation (27) does not contain a source term associated with PUI driving since the fluctuations are Alfvénic. We note too that, unlike the slab formulation used in Zank et al. (2017) and Adhikari et al. (2017), stream-shear source terms are present. In applying the NI MHD turbulence transport theory to the problem of cosmic ray mfps in the supersonic solar wind, Zhao et al. (2017) found that the cosmic ray diffusion coefficients calculated without a slab stream-shear source are much larger than the values observed (Palmer 1982; Reames 1999). Accordingly, they therefore included the stream-shear source in the slab model to obtain reasonable cosmic ray diffusion coefficient values. In view of the Zhao et al. (2017) result, we include an appropriate stream-shear source term in the slab model equations.

The incorporation of dissipative heating via turbulence is incorporated in the 1D thermal plasma temperature transport equation through (Adhikari et al. 2015)

$$
U\frac{dT_s}{dr} + (\gamma_s - 1)T_s\frac{1}{r^2}\frac{d}{dr}(r^2U) = \frac{1}{2}\nu_c^s T_s + \frac{(\gamma_s-1)}{2n_s k}S_t,
\tag{30}
$$

where $\gamma_s = 5/3$ is the adiabatic index, m_p the proton mass, and k Boltzmann's constant. This equation is derived directly from the thermal pressure Equation (19) after assuming the ideal gas law, $P_s = 2n_s kT_s$ and equal proton and electron temperatures. The turbulent heating term for the thermal plasma is given by

(Hossain et al. 1995; Verdini et al. 2010; Adhikari et al. 2015)

$$S_t = m_p n_s \alpha \Bigg[\frac{2\langle z^{*+2}\rangle \langle z^{\infty -2}\rangle^{1/2}}{\lambda_\infty^+} + \frac{2\langle z^{*-2}\rangle \langle z^{\infty +2}\rangle^{1/2}}{\lambda_\infty^-} + E_D^* \left(\frac{\langle z^{\infty -2}\rangle^{1/2}}{\lambda_\infty^+} + \frac{\langle z^{\infty +2}\rangle^{1/2}}{\lambda_\infty^-} \right) + 2\frac{\langle z^{\infty +2}\rangle \langle z^{\infty -2}\rangle^{1/2}}{\lambda_\infty^+} + 2\frac{\langle z^{\infty -2}\rangle \langle z^{\infty +2}\rangle^{1/2}}{\lambda_\infty^-} + E_D^\infty \left(\frac{\langle z^{\infty -2}\rangle^{1/2}}{\lambda_\infty^+} + \frac{\langle z^{\infty +2}\rangle^{1/2}}{\lambda_\infty^-} \right) \Bigg], \tag{31}$$

and α is the von Kármán–Taylor constant, taken here to be $\alpha = 0.2$. That it is only the thermal plasma that is heated dissipatively by low-frequency turbulence is not entirely obvious, but we suppose that the dissipation scale is where heating of the plasma occurs, i.e., at the end of the turbulent cascade in wave number space. The implication is that the dissipation is due to the interaction of very large k (very small-scale) fluctuations with the background protons. Since the dissipation has to be some form of wave/fluctuation-particle interaction that occurs on such small scales, the protons cannot be very energetic (unlike the 1 keV PUI protons), i.e., only particles that have rather small speeds v can interact with the very small-scale fluctuations. Recall that the PUI distribution is a (possibly filled) shell distribution centered on zero—see for example, Figure 3.2 in Zank (1999)—in the solar wind frame. Because the turbulence is advected in the background solar wind flow, we need to consider the dissipation of turbulence in that frame. Consequently, the only cold protons that are accessible at the end of the turbulent cascade are solar wind protons, since the PUIs have energies $\sim$1 keV due to pickup. Of course, with adiabatic cooling, there may be some fraction of colder PUIs that will be heated by turbulent dissipation, but it is unlikely to affect the $>10^6$ K mean temperature of the PUIs. Hence, we interpret this to mean that it is the core thermal solar wind protons that experience the turbulent dissipative heating and not the hotter PUIs. The PUIs can of course gain energy through, e.g., second-order Fermi acceleration instead, so they can provide a dissipative avenue too, but of a different kind. We do not consider this latter possibility since it is related to the possible acceleration of PUIs, which is distinct from the turbulence considered here.

Since the SWAP instrument suite can measure the thermal solar wind density variance in the distant heliosphere, we consider too the heliocentric evolution of the fluctuating density variance $\langle \rho_s^{\infty 2}\rangle$ in the NI MHD formalism (Hunana & Zank 2010). The steady form of the density variance transport equation is (Zank et al. 2012b, 2017; Adhikari et al. 2017)

$$U\frac{d}{dr}\langle \rho_s^{\infty 2}\rangle - 2\langle \rho_s^{\infty 2}\rangle \langle u^{\infty 2}\rangle^{1/2}\frac{1}{\rho_s}\frac{d\rho_s}{dr} + 2\langle \rho_s^{\infty 2}\rangle \times \left(\frac{2U}{r} + \frac{dU}{dr}\right) = -\frac{\langle u^{\infty 2}\rangle^{1/2}\langle \rho_s^{\infty 2}\rangle}{\ell_u^\infty} + \eta_1 \langle \rho_s^{\infty 2}\rangle_0 \frac{r_0^2|\Delta U|}{r^3} + \eta_2 \langle \rho_s^{\infty 2}\rangle_0 \times \frac{U}{V_A}\frac{n_{\rm H}^\infty}{\tau_{\rm ion}^0 n_{SW}^0}\exp\left(\frac{-L}{r}\right). \tag{32}$$

Here, we have introduced two source terms for the density fluctuations, one associated with their possible excitation by stream shear with a strength η_1 and the other with fluctuations associated with the pickup process (Adhikari et al. 2017; Zank et al. 2017). The variance in the quasi-2D velocity fluctuations $\langle u^{\infty 2}\rangle$ is present in Equation (32), together with the correlation length $\ell_{\rm u}$ for the velocity fluctuations. The equations describing the evolution of $\langle u^{\infty 2}\rangle$ and $\ell_{\rm u}$ are derived from Equations (22)–(29). Indeed, the following useful quantities can be derived from the turbulence variables above:

$$E_T^{\infty,*} \equiv \frac{\langle z^{\infty,*+2}\rangle + \langle z^{\infty,*-2}\rangle}{2} = \langle u^{\infty,*2}\rangle + \langle B^{\infty,*2}/\mu_0\rho_s\rangle;$$
$$E_C^{\infty,*} \equiv \frac{\langle z^{\infty,*+2}\rangle - \langle z^{\infty,*-2}\rangle}{2} = 2\langle \boldsymbol{u}^{\infty,*}\cdot \boldsymbol{B}^{\infty,*}/\sqrt{\mu_0\rho_s}\rangle;$$
$$r_A^{\infty,*} \equiv \frac{\langle u^{\infty,*2}\rangle}{\langle B^{\infty,*2}/\mu_0\rho_s\rangle} = \frac{E_T^{\infty,*} + E_D^{\infty,*}}{E_T^{\infty *} - E_D^{\infty,*}};$$
$$\langle u^{\infty,*2}\rangle = \frac{E_T^{\infty,*} + E_D^{\infty,*}}{2}; \quad \left\langle \frac{B^{\infty,*2}}{\mu_0\rho_s}\right\rangle = \frac{E_T^{\infty,*} - E_D^{\infty,*}}{2};$$
$$\ell_u^\infty = \frac{(E_T^\infty + E_C^\infty)\lambda_\perp^+ + (E_T^\infty - E_C^\infty)\lambda_\perp^- + E_D^\infty \lambda_D^\infty}{2(E_T^\infty + E_D^\infty)};$$
$$\ell_b^\infty = \frac{(E_T^\infty + E_C^\infty)\lambda_\perp^+ + (E_T^\infty - E_C^\infty)\lambda_\perp^- - E_D^\infty \lambda_D^\infty}{2(E_T^\infty - E_D^\infty)}. \tag{33}$$

In the above, E_T denotes the total energy in either the quasi-2D or slab components, E_C the cross-helicity, often expressed as the normalized cross-helicity $\sigma_c \equiv E_c/E_T$, $r_{\rm A}$ is the Alfvén ratio, $\sigma_D \equiv E_D/E_T$ the normalized residual energy, and $\ell_{\rm b}$ the correlation length for fluctuating magnetic field variance.

PUIs both drive turbulence in the distant heliosphere as well as decelerate the bulk solar wind flow through the transferal of momentum and energy to the PUIs themselves, and they form a thermally dominant non-equilibrated suprathermal plasma component. The driving of turbulence by PUIs leads indirectly to the heating of the thermal solar wind plasma. This complicated coupling of the bulk solar wind, low-frequency solar wind turbulence, and the PUI distribution is captured by the model Equations (14)–(17), (19)–(21), and (22)–(32).

3. Evolution of the Solar Wind from 1–75 au

The Equations (14)–(17), (19)–(21), and (22)–(32) that describe the evolution of the bulk solar wind and the associated turbulence are solved from 1–75 au. Over this large distance, the PUI heat conduction and viscous terms can safely be neglected for a steady-state model, i.e., we set both $K_{rr} = 0$ and $\Pi_{p_{rr}} = 0$ in this section. For an unsteady model in which, e.g., shocks are present, then the heat conduction and viscous terms should not be neglected since they determine the individual shock characteristics (structure, heating of PUIs and thermal gas, for example). The predicted steady-state solutions are compared to both *Voyager* 2 plasma and magnetometer data and NH plasma data. The boundary values that we assumed at 1 au are tabulated in Table 1 and the assumed values of the various parameters that enter the turbulence transport equations are listed in Table 2.

The panels plotted in Figure 1 depict the large-scale plasma variables (the number density, radial component of the flow

Table 1
Boundary Values at 1 ($\equiv r_0$) au for the Thermal Plasma, Magnetic Field, and Turbulence Variables

Quasi-2D Core Model Equations		Slab Model Equations	
$\langle z^{\infty +2}\rangle$	1600 km^2 s^{-2}	$\langle z^{*+2}\rangle$	400 km^2 s^{-2}
$\langle z^{\infty -2}\rangle$	160 km^2 s^{-2}	$\langle z^{*-2}\rangle$	40 km^2 s^{-2}
E_D^{∞}	-80 km^2 s^{-2}	E_D^{*}	-20 km^2 s^{-2}
L_{∞}^{+}	2.95×10^9 km^3 s^{-2}	L_{*}^{+}	2.95×10^8 km^3 s^{-2}
L_{∞}^{-}	2.65×10^8 km^3 s^{-2}	L_{*}^{-}	1.66×10^8 km^3 s^{-2}
L_D^{∞}	-1.7×10^8 km^3 s^{-2}	L_D^{*}	-4.22×10^7 km^3 s^{-2}
$\langle \rho_s^{\infty 2}\rangle$	3.5 cm^{-6}		
U	440 km s^{-1}		
n_s	7 cm^{-3}		
n_p	$3 \times 10^{-4}\, n_{\rm H}^{\infty} \exp(-L/r_0)$ cm^{-3}		
P_s	10^{-11} kg m^{-1} s^{-2} (Pa)		
P_p	$2.7 \times 10^{-14}\, n_{\rm H}^{\infty} \exp(-L/r_0)$ kg m^{-1} s^{-2} (Pa)		

Table 2
Model Parameters That Enter Equations (14)–(17), (19)–(21), and (22)–(32)

Parameters	Values	Parameters	Values
b	0.22	ν_{p0}	1.5×10^{-7} s^{-1}
$C_{\rm sh}^{+}$	0.45	$\tau_{\rm ion}^{0}$	10^6 s
$C_{\rm sh}^{-}$	0.45	$n_{\rm sw}^{0}$	5 cm^{-3}
$C_{\rm sh}^{E_D}$	-0.25	$n_{\rm H}^{\infty}$	0.1 cm^{-3}
$C^{*+}_{\rm sh}$	0.16	$U_{\rm H}$	20 kms^{-1}
$C^{*-}_{\rm sh}$	0.16	$T_{\rm H}$	6500 K
$C^{*E_D}_{\rm sh}$	-0.1	η_1	1.8×10^{-2}
f_D	0.18	η_2	5×10^{-3}
ΔU	200 km s^{-1}	α	0.2
V_{A0}	54 km s^{-1}	ν_{c0}	2×10^{-15} cm^2
L	7 au		

velocity, the pressure, and the temperature) as a function of heliocentric distance r. The solid black curves denote thermal solar wind quantities and the red PUI quantities. The blue plus symbols denote *Voyager* 2 observations from 1–75 au, the green plus symbols denote NH SWAP measurements of the thermal solar wind, and the red plus symbols the NH SWAP measurements of PUIs. A detailed discussion describing the data analysis used for the *Voyager* 2 observations can be found in Adhikari et al. (2015, 2017), and this analysis was extended to the SWAP data. Each panel comprises two plots, and each plot shows the theoretically predicted results. The top plot of each panel shows *Voyager* 2 data from 1–75 au and the lower plot shows NH SWAP data from 11.26–38 au. The two data sets are completely independent but we illustrate the spatial region where they overlap. We emphasize that the same theoretical model derived curves are used in all plots.

The solar wind and PUI number densities exhibit the well-known radial heliocentric dependence ($n_s \propto r^{-2}$, and n_p increases to a maximum value at ~12 au and then very slowly decreases as the solar wind expands radially outward) (Holzer 1972; Isenberg 1986; Khabibrakhmanov et al. 1996; Zank 1999). The model and observations match well overall. Some solar cycle dependence is exhibited in the thermal plasma density, but this is more evident in the *Voyager* 2 velocity profile. Shorter timescale variation is present in the PUI density observations, most likely associated with interplanetary shocks or streams.

The top right and bottom left panels of Figure 1 plot the theoretical thermal and PUI pressures and temperatures, respectively. Both the thermal pressure and temperature are interesting in that they exhibit a change in the rate of cooling at ~20 au. As has been discussed already (Williams et al. 1995; Matthaeus et al. 1999; Smith et al. 2001; Breech et al. 2008; Isenberg et al. 2010; Adhikari et al. 2015, 2017), the inclusion of the additional dissipation associated with the driving of turbulence by PUIs (Zank et al. 1996) is responsible for the heating of the outer heliospheric thermal plasma. The importance of this additional heating by turbulence can be seen from the dashed line curves plotted in the pressure and temperature panels of Figure 1. The dashed lines show the thermal pressure and temperature profiles in the absence of turbulent heating. The difference between the theoretical curves (and observations) with and without turbulent heating is quite striking. The agreement between the theoretical and observed *Voyager* 2 pressure and temperature is very good. A slow flattening in the thermal pressure profile, while not as evident in the NH SWAP data, appears to be consistent with the predicted flattening shown by the model, as does the thermal plasma temperature increase. Both the PUI pressure and temperature are clearly consistent with those observed, the PUI temperature being more than two orders of magnitude higher than that of the thermal pressure.

One interesting point about the temperature plots is that our model assumes explicitly that the dissipation of PUI-driven turbulence occurs only in the thermal plasma, i.e., the dissipation of low-frequency turbulence does not heat the PUIs. However, the PUI temperature and pressure plots do indicate a turn-up in the PUI temperature near 38 au, and this is not consistent with the model presented here. We do not introduce a turbulence dissipation or heating term into the PUI temperature equation, as we do for the core thermal solar wind ions, for the reasons outlined above. There appear to be several possible explanations for a PUI increase in temperature. The first is that we do not understand the nature of turbulent heating in a non-equilibrated plasma system, and it may be entirely possible that the hotter distribution of PUIs may experience some heating despite their already high temperature. A second and perhaps more plausible explanation may be that the PUIs are further energized by some form of second-order Fermi acceleration related to counter-propagating Alfvén waves (Bogdan et al. 1991; Le Roux & Ptuskin 1998). A third possibility is that some form of further acceleration of PUIs related to the preferential reflection and subsequent energization of PUIs by interplanetary shocks (Zank et al. 1996), as has been observed by the SWAP instrument (Zirnstein et al. 2018), may account for the observed increase in the PUI temperature.

Solar wind variation is clearly evident in the solar wind speed plot. The theoretical radial velocity plots show the well-known expected gradual deceleration of the solar wind due to charge exchange (Wallis 1971; Holzer 1972; Isenberg et al. 1985; Isenberg 1986; Khabibrakhmanov et al. 1996; Zank 1999), which is not easily discerned from the observations—however, see the analysis presented by Richardson et al. (2004).

Figure 2 shows plots of various turbulence quantities predicted by the model and compared to the corresponding values derived from *Voyager* 2 observations (see Adhikari et al. 2017) from 1–75 au. All these plots require magnetic field data, which unfortunately NH cannot provide. These plots are shown

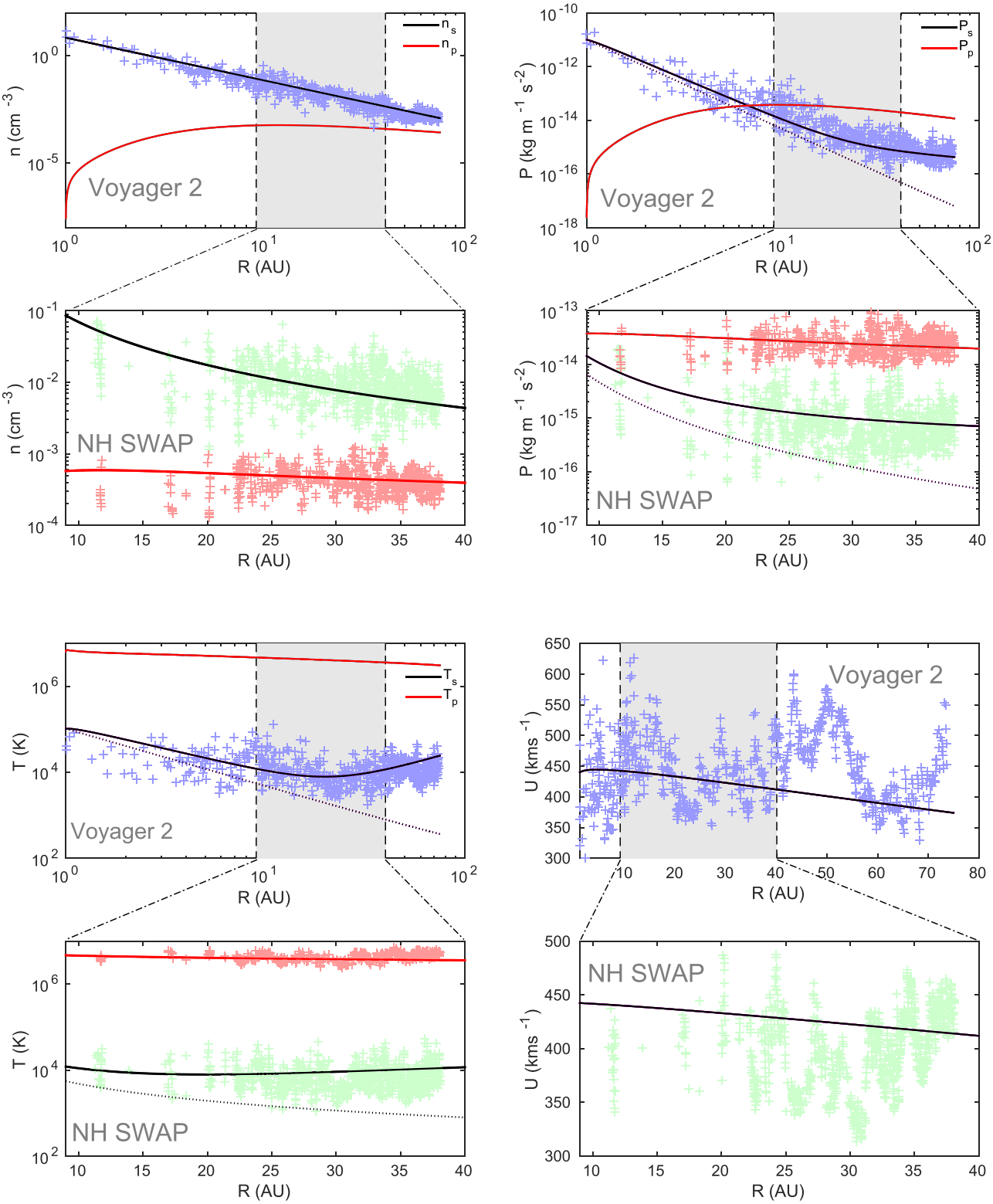

Figure 1. Plots of the theoretical model are compared to the bulk or background plasma observations from the *Voyager* 2 plasma instrument taken between 1 and 75 au (top plots of each panel) and from the NH SWAP instrument between 11.26 and 38 au (lower expanded plots of each panel). Top left: curves showing the predicted large-scale background thermal plasma number density n_s (black curve) and the predicted PUI number density n_p (red curve) together with the *Voyager* 2 observed thermal plasma number density (top plot) and the NH SWAP observed thermal plasma number density and PUI number density (bottom plot). Top right: predicted thermal plasma and PUI pressure plots compared with the thermal pressure observed by *Voyager* 2 (top), and the thermal and PUI pressure observed by NH SWAP (bottom). The dotted lines in the upper plot show pressure solutions in the absence of turbulent heating. Bottom left: Predicted temperature plots of the thermal background plasma (black line) and PUIs (red line) compared to *Voyager* 2 observations (top), and compared to NH SWAP observations (bottom). The dotted lines in the upper plot show temperature solutions in the absence of turbulent heating. Bottom right: Predicted background solar wind radial speed U compared to that observed by *Voyager* 2 (top) and NH SWAP (bottom).

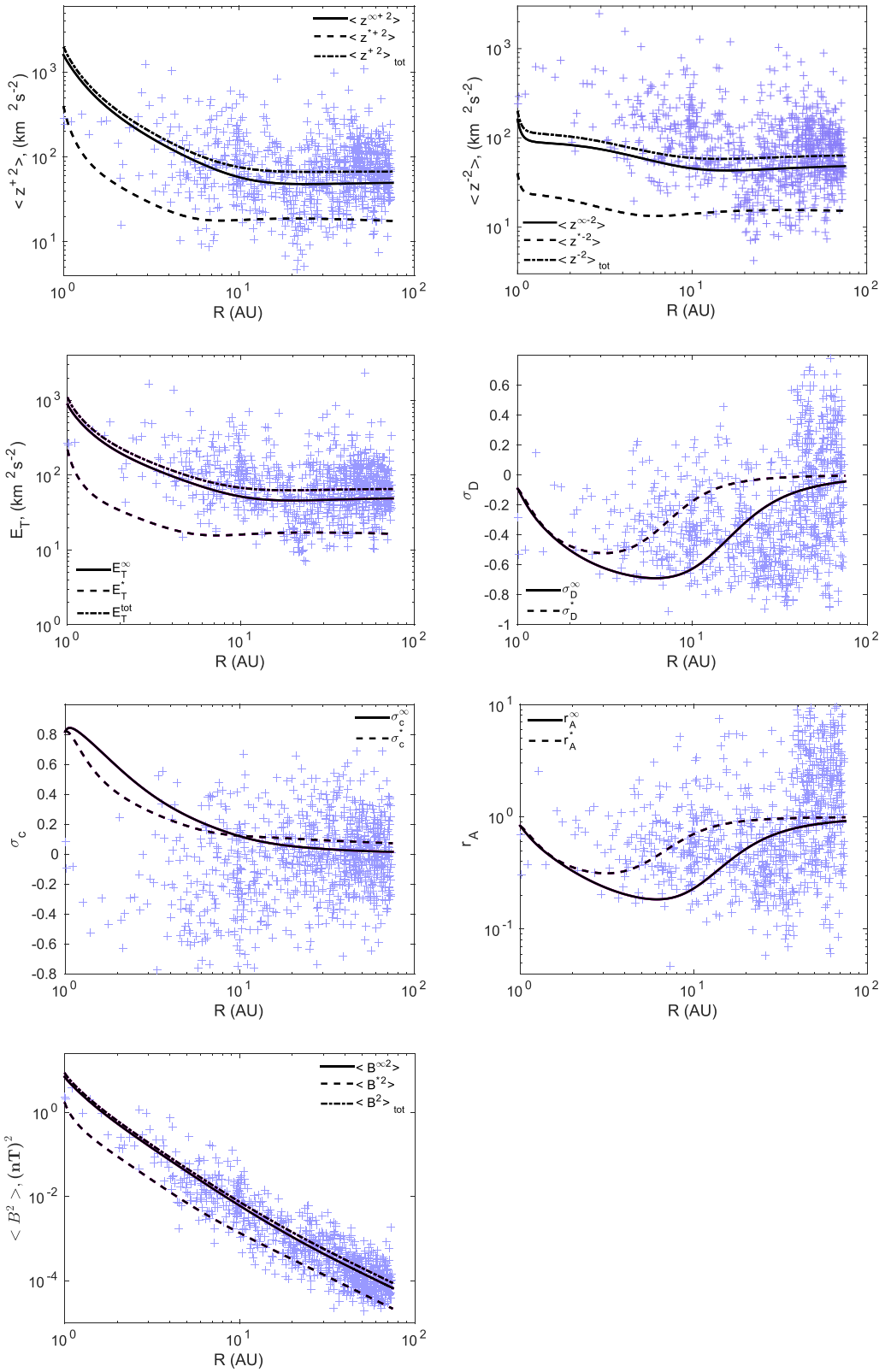

Figure 2. Various turbulence quantities and their comparison with *Voyager* 2 derived observations based on the parameters used in Figure 1. Top left: variance of the outward propagating Elsässer variable energy density, $\langle z^{+2}\rangle$. Solid and dashed curves correspond to 2D and slab turbulence quantities, respectively, and the dashed-dotted curve to the sum of 2D and slab quantities. Top right: variance of the inward propagating Elsässer variable energy density, $\langle z^{-2}\rangle$. Second panel down, left: total energy in turbulent fluctuations $E_T = (\langle z^{+2}\rangle + \langle z^{-2}\rangle)/2$. The 2D (solid line), slab (dashed), and total (dashed-dotted) components are plotted. Second panel down, right: normalized residual energy σ_D for 2D and slab components. Third panel down, left: normalized cross-helicity σ_c for 2D (solid) and slab turbulence (dashed). Third panel down, right: Alfvén ratio r_A for 2D and slab turbulence components. Bottom left: the variance in magnetic field fluctuations $\langle B^2\rangle$ for the 2D (solid), slab (dashed), and total (dashed-dotted), i.e., the magnetic energy density.

in part for completeness since this particular model, additionally constrained by the SWAP thermal plasma and PUI observations, is a little different from that presented by Adhikari et al. (2017). In deriving their model solutions for transport of turbulence throughout the heliosphere, Adhikari et al. (2017) assumed that the background radial solar wind speed U was constant. Of course, as we have seen, the inclusion of PUIs in the solar wind yields a gradual deceleration of the solar wind radial speed, together with corresponding modifications to the background density and magnetic field. Inevitably, the heliocentric dependence on these background variables has an effect on the detailed transport of turbulence, and this is illustrated in Figure 2. A side-by-side comparison of the corresponding figures in Adhikari et al. (2017) with those of Figure 2 illustrates the differences quite clearly. We mention a few briefly below.

The top two plots of Figure 2 show the energy density in the forward and backward Elsässer variables. The solid lines show the majority 2D component and the dashed lines the minority slab turbulence contribution. The sum or total energy density is depicted by the dashed-dotted line. As usual, the blue symbols are values derived from *Voyager* 2 observations. There is little difference between the Adhikari et al. (2017) and the Figure 2 evolution of the majority quasi-2D component qualitatively or quantitatively. However a clear difference in the evolution of the slab turbulence is apparent for both forward and backward Elsässer energies. The pronounced minimum at about ∼4 au that is present when a constant radial solar wind flow speed is assumed is essentially absent when the solar wind is mediated by PUIs. Similar remarks apply to the total energy E_T. The normalized residual energy σ_D is similar qualitatively to that presented by Adhikari et al. (2017), but quantitative differences in both the evolution of the quasi-2D and slab components are apparent, with, in both cases, a slower decrease toward a magnetically dominated state within ∼3 au, is due to the inclusion of shear driving of the slab turbulence. Similar comments hold for the Alfvén ratio $r_{\rm A}$. The normalized cross-helicity σ_c results are a little different, particularly within 3–4 au, but this may stem simply from using slightly different boundary values at 1 au and the inclusion of shear driving of slab turbulence. We note that the slab turbulence, even when driven directly by the creation of PUIs in the outer heliosphere, remains very much a minority component compared to the quasi-2D turbulence. The differences in behavior that indirectly affect the quasi-2D component through the appropriate source terms are evident in the σ_c, σ_D, and $r_{\rm A}$ slab turbulence plots. This gives a quite complete characterization of the macroscopic turbulence state throughout the heliosphere. The bottom panel illustrates the radial dependence of the fluctuating magnetic field variance, indicating that theory and observations are consistent, which is now a well-known result (Zank et al. 1996; Matthaeus et al. 1999; Smith et al. 2001). Further discussion of plots like those in Figure 2 can be found in Zank et al. (2017) and Adhikari et al. (2017), the latter of which also provide as full description of the data analysis.

Fluctuating thermal plasma quantities and the correlation functions are plotted in Figure 3. As in Figure 1, the top plots of each panel show results from 1–75 au, and the bottom plots from 11.26–38 au. The top left panel shows the theoretical density variance $\langle \rho_s^{\infty 2} \rangle$, which appears to match the derived *Voyager* 2 observations rather well, but seems to underestimate slightly the SWAP-derived values. A very slight bump can be seen in the theoretical plot of the density variance, which is not exhibited in the corresponding plot shown in Adhikari et al. (2017). This is because we use slightly different values for the parameters η_1 and η_2 here and no physical significance should be ascribed to the bump. The top right panel shows the variance in velocity fluctuations, for the majority 2D, minority slab, and total fluctuating fields. The velocity variance observations exhibit quite a large scatter. The theoretical curves appear to be a little higher than the observed SWAP values, although not significantly. Part of the reason for the small differences between the model and the variances derived from the SWAP data may be related to our using a single set of boundary values (Table 1) to compare to the *Voyager* 2 and NH data sets. The *Voyager* 2 observations are taken from 1983–1992 and those of NH from 2008–2017 for the radial heliocentric distance interval 11–38 au. The solar cycle observed by NH was much weaker than that observed over this distance interval by *Voyager* 2 (Lockwood et al. 2011; Zhao et al. 2014; Zhao & Zhang 2015).

It is quite possible that some of the Table 1 boundary values should be adjusted to better reflect the solar wind conditions at the time the SWAP observations were made. The solar wind radial speed correlation length is plotted in the lower left panels. The correlation length of the velocity fluctuations is calculated from the 2 minutes resolution SWAP data, which is only available around ∼32.78 and 37 au. The lower resolution data did not provide as good results. Finally, the bottom right panel shows the correlation functions for the quasi-2D and slab turbulence. The $L_\infty^\pm$ and $L_*^\pm$ correlation lengths are all positive, whereas the L_D^∞ and L_D^* are both negative functions from 1–75 au. Notice that L_D^∞ is a minimum at the same heliocentric location as the quasi-2D residual energy E_D^∞ is a minimum. The same is true of L_D^* and E_D^*.

Finally, for completeness again, we plot in Figure 4 the various correlation lengths pertaining to the magnetic field and compare them to values derived from the *Voyager* 2 observations. For further details, we refer the reader to Adhikari et al. (2017).

4. The PUI-mediated HTS

The model Equations (14)–(17), (19)–(21), and (22)–(32) provide us with the boundary conditions upstream of the HTS. In this section, we solve the model equations to a heliocentric distance of 84 au, the distance at which *Voyager* 2 crossed the HTS, and use the plasma values to compute the expected structure of the quasi-perpendicular HTS when mediated by PUIs. The upstream HTS boundary conditions are listed in Table 3.

The basic equations governing the structure of shocks mediated by PUIs were derived by Zank et al. (2014, 2016) and Zank (2016) and used by Mostafavi et al. (2017b) to examine the structure of energetic particle-mediated shock waves, including the HTS. Of particular importance is that the non-isotropic PUI distribution introduces both a collisionless heat flux and viscosity that provides the basic dissipation that governs the structure of shock waves.

The one-dimensional continuity, momentum and pressure equations governing the non-thermal PUIs and the isotropic thermal background gas are given by (Zank et al. 2014, 2016;

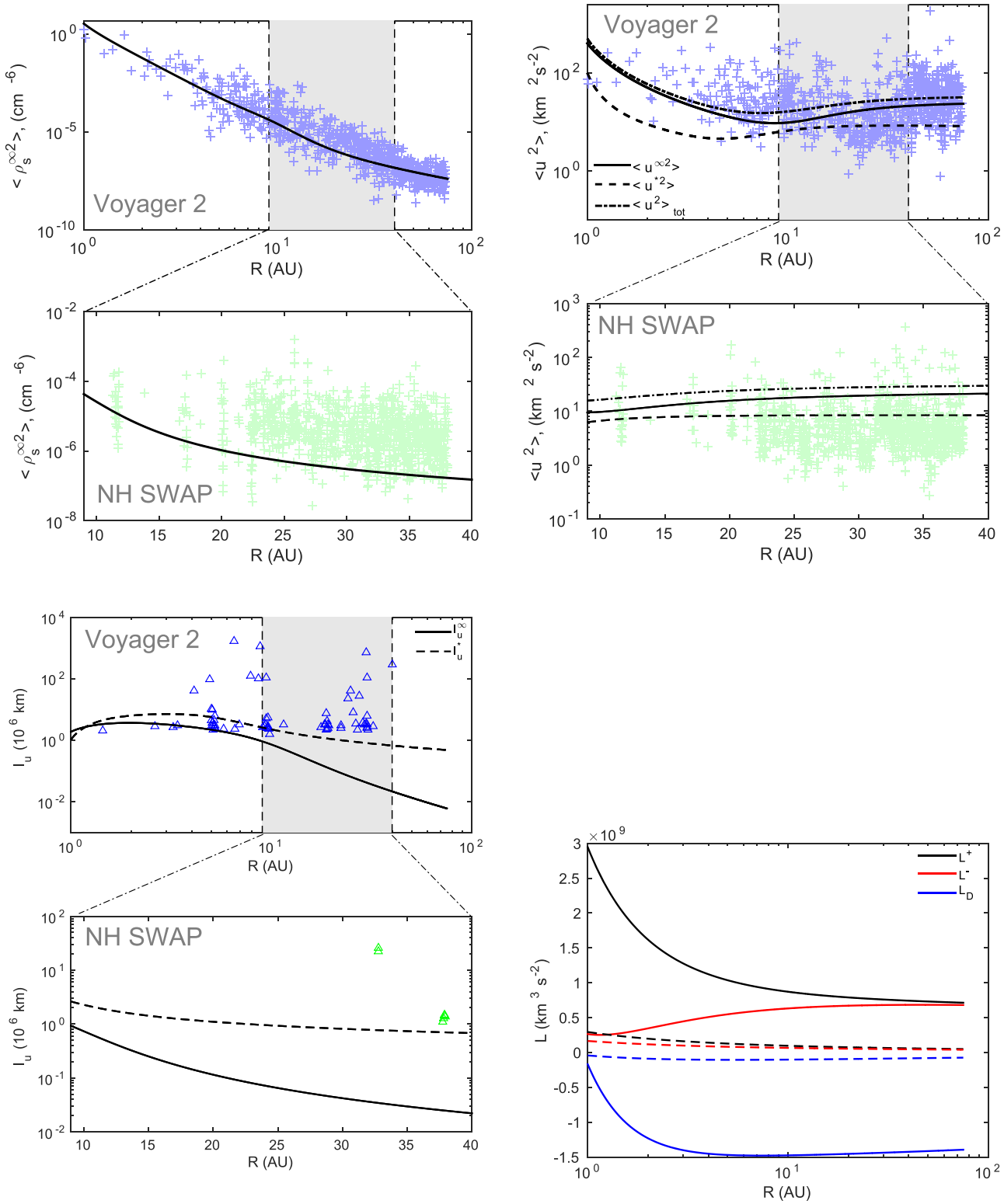

Figure 3. Same format as Figure 1. Comparison of predicted plasma turbulence quantities that can be compared to those evaluated from *Voyager* 2 (upper plot of each panel) and NH SWAP (lower plot of each panel) observations. Top left: the variance in thermal solar wind density fluctuations $\langle \rho_s^{\infty 2} \rangle$ compared to *Voyager* 2 and NH SWAP observations. Top right: the variance in velocity fluctuations $\langle u^2 \rangle$ for the 2D (solid), slab (dashed), and total (dashed-dotted), i.e., the kinetic energy density, compared to *Voyager* 2 and NH SWAP observations. Bottom left: plot of the predicted correlation length for velocity fluctuations ℓ_u compared to that derived from *Voyager* 2 and NH SWAP observations. Bottom right: plot of the theoretical correlation functions $L_\infty^{\pm}$, $L_*^{\pm}$, and $L_D^{\infty,*}$ for the quasi-2D and slab turbulence components.

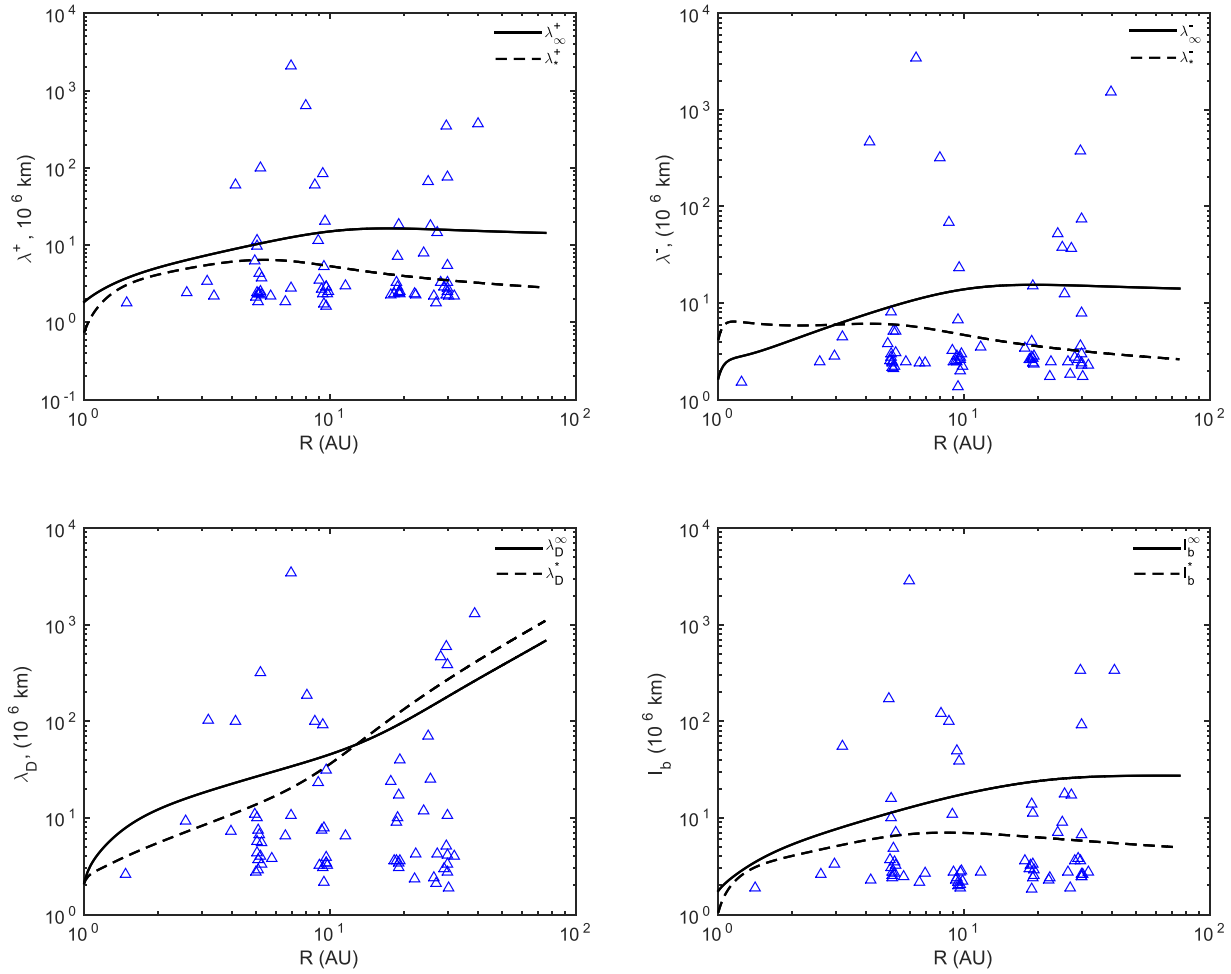

Figure 4. Plots of the various correlation lengths that involve the magnetic field compared to those derived from *Voyager* 2 observations. Top left: correlation lengths λ^+ for quasi-2D (solid line) and slab (dashed line) turbulence. Top right: correlation lengths $\lambda^-$for quasi-2D (solid line) and slab (dashed line) turbulence. Bottom left: correlation lengths λ_D for quasi-2D (solid line) and slab (dashed line) turbulence. Bottom right: correlation lengths ℓ_b for quasi-2D (solid line) and slab (dashed line) turbulence.

Table 3
Boundary Conditions Upstream of the HTS Derived from the Solar Wind Model Evaluated at 84 au and the Corresponding Downstream State Obtained by Solving the PUI-mediated Rankine–Hugoniot Conditions (Mostafavi et al. 2017b)

HTS at 84 au		
Parameters	Upstream	Downstream
Total density (cm^{-3})	0.00125674	0.0034303975
Thermal gas temperature (K)	2.8397×10^4	1.514×10^5
PUI temperature (K)	3.0256×10^6	2.6828×10^7
Thermal solar wind pressure ($kg\,m^{-1}\,s^{-2}$)	3.933×10^{-16}	2.09703×10^{-15}
PUI pressure ($kg\,m^{-1}\,s^{-2}$)	1.0478×10^{-14}	9.290763×10^{-14}
Magnetic pressure ($kg\,m^{-1}\,s^{-2}$)	2.485074×10^{-15}	1.851498×10^{-14}

Zank 2016; Mostafavi et al. 2017b)

$$\frac{\partial \rho}{\partial t} + \frac{\partial (\rho U)}{\partial x} = 0; \tag{34}$$

$$\rho\left(\frac{\partial U}{\partial t} + U\frac{\partial U}{\partial x}\right) = -\frac{\partial P_s}{\partial x} - \frac{\partial P_p}{\partial x} - \frac{1}{\mu_0}B_y\frac{\partial B_y}{\partial x} - \frac{\partial \Pi_p}{\partial x}; \tag{35}$$

$$\frac{\partial P_s}{\partial t} + U\frac{\partial P_s}{\partial x} + \gamma_s P_s \frac{\partial U}{\partial x} = 0; \tag{36}$$

$$\frac{\partial P_p}{\partial t} + U\frac{\partial P_p}{\partial x} + \gamma_p P_p \frac{\partial U}{\partial x} = \frac{1}{3}\frac{\partial}{\partial x} \times \left(K_p \frac{dP_p}{dx}\right) - (\gamma_p - 1)\Pi_p \frac{\partial U}{\partial x}; \tag{37}$$

where ρ is the total density (sum of PUI and thermal gas density) and the collisionless PUI viscosity Π_p and heat flux K_p transport coefficients are included (for more details see Zank et al. 2014; Zank 2016; Mostafavi et al. 2017a, 2017b). The one-dimensional form of the viscosity term for a perpendicular shock may be expressed as $\Pi_p = -\frac{1}{3}\eta_p \frac{dU}{dx}$ (Mostafavi et al. 2017b; Mostafavi & Zank 2018). η_p is the coefficient of the PUI collisionless viscosity and can be approximated as $P_p\tau_s$, where τ_s is a characteristic scattering time for PUIs by slab

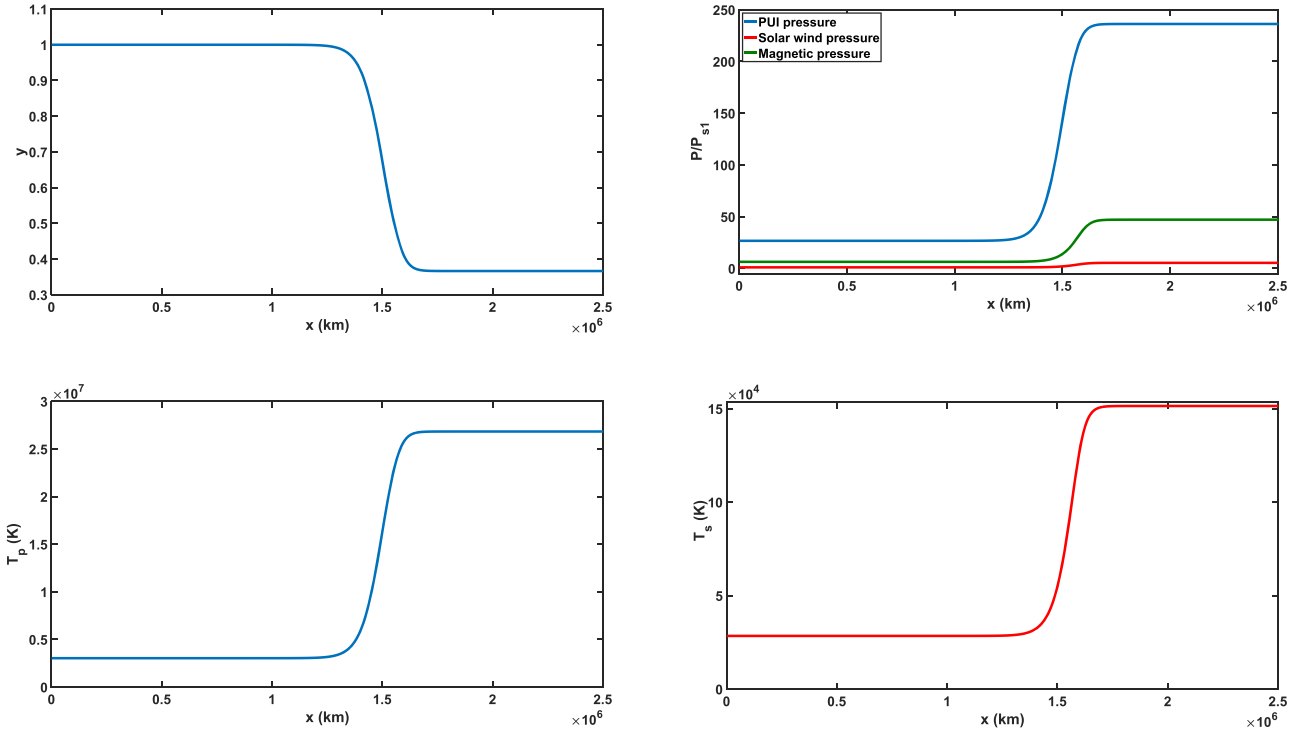

Figure 5. Smoothed shock transition corresponding to model derived upstream HTS parameters when both the PUI heat flux and viscosity are included. Top left: inverse compression ratio showing the smoothed shock. Top right: PUI, thermal gas, and magnetic pressure normalized to the thermal gas pressure far upstream. Bottom left: the PUI temperature through the shock as a function of distance. Bottom right: the thermal gas temperature through the shock as a function of distance. Here, $\gamma_s = 5/3$, $\gamma_p = 5/3$, $P_{p1}/P_{s1} = 26.636$, $y_B = B_{y1}^2/(\mu_0 \rho_1 U_{x1}^2) = 0.03144$, where y_B is the square of the inverse Alfvénic Mach number of the flow far upstream of the shock, and $M_{s1} = \sqrt{\rho_1 U_{x1}^2/\gamma_g P_{g1}} = 15.527$ is the thermal gas Mach number far upstream.

turbulence (Zank et al. 2014). We assume constant values for the PUI heat flux and viscosity coefficients, being given by $K_p = 3.38 \times 10^{13}$ m^2 s^{-1} and $\eta_p = 2.76 \times 10^{-12}$ kg/ms, for simplicity. This yields a Schmidt number ($=\eta_p/\rho_1 K_p$) of 0.038. We neglect the PUI source terms through the shock.

From the conservation form of Equations (34)–(37), we can determine the downstream state from the upstream state of the solar wind at 84 au as derived from our solar wind model. Both the upstream and related downstream states are tabulated in Table 3. The shock structure Equations (34)–(37) allow us to compute the structure of the HTS when mediated by PUIs, connecting the upstream to the downstream state. Illustrated in Figure 5 is the shock transition showing that PUIs completely mediate and smooth the shock over a scale length $\sim K_p/U_1$ (where U_1 is the upstream flow speed), which, from Figure 5, is found to be about 3.5×10^5 km. Such a shock thickness is consistent with observations of the second of the *Voyager* 2 termination shock crossings, TS-2, that showed the thickness of the TS-2 shock was $\sim 3 \times 10^5$ km (Richardson et al. 2008). The top left panel shows the inverse compression ratio, indicating that the HTS is relatively weak with a compression ratio of ∼2.73. This value is a little larger than quoted by Burlaga et al. (2008) in their estimate of the HTS compression ratio. The top right panel plots the normalized PUI, thermal gas, and magnetic field ($B^2/2\mu_0$) pressures through the HTS. The pressures are clearly dominated by the PUI component, and the upstream ram energy of the supersonic solar wind is converted primarily to heating the PUIs. The thermal plasma remains relatively cold. Downstream of the HTS, the thermal gas temperature is predicted to be $\sim 1.514 \times 10^5$ K, consistent with *Voyager* 2 measurements of the downstream thermal plasma temperature (Richardson 2008; Richardson et al. 2008) versus a downstream PUI temperature of $\sim 2.6828 \times 10^7$ K. The latter temperature is consistent with the kinetic estimate derived by Zank et al. (2010) based on the preferential reflection of PUIs by the HTS cross-shock potential (Zank et al. 1996).

5. Transmission and Generation of Solar Wind Turbulence through the HTS

Having determined the structure of the PUI-mediated HTS, we can use the predicted upstream turbulence conditions to determine the transmission and generation of turbulence downstream of the HTS. To address this problem, we solve the 1D form of the turbulence transport equations of Zank et al. (2017) in a planar geometry through the flow structure of the HTS determined in Section 4. This is closely related to the investigation by Adhikari et al. (2016a, 2016b) of the interaction of solar wind turbulence with shocks in a high plasma beta regime, except here extended to a two-component quasi-2D–slab turbulence model.

The relevant stationary 1D equations for the quasi-2D component of the turbulence may be expressed as

$$U\frac{d\langle z^{\infty\pm 2}\rangle}{dx} + \frac{1}{2}\frac{dU}{dx}\langle z^{\infty\pm 2}\rangle + \frac{1}{2}\frac{dU}{dx}E_D^{\infty} - \frac{1}{2}(\langle z^{\infty\pm 2}\rangle - E_D^{\infty})\langle z^{\infty\pm 2}\rangle^{1/2}\frac{1}{\rho_s}\frac{d\rho_s}{dx} = -2\frac{\langle z^{\infty\pm 2}\rangle\langle z^{\infty\mp 2}\rangle^{1/2}}{\lambda_{\infty}^{\pm}} + 2\frac{\langle z^{*\pm 2}\rangle\langle z^{*\mp 2}\rangle^{1/2}}{\lambda_{*}^{\pm}}; \quad (38)$$

$$U\frac{dE_D^{\infty}}{dx} + \frac{1}{2}\frac{dU}{dx}E_D^{\infty} + \frac{1}{2}\frac{dU}{dx}E_T^{\infty} - \frac{1}{4}(E_D^{\infty} - \langle z^{\infty+2}\rangle^{1/2}\langle z^{\infty-2}\rangle^{1/2})(\langle z^{\infty+2}\rangle^{1/2} + \langle z^{\infty-2}\rangle^{1/2}) \times \frac{1}{\rho_s}\frac{d\rho_s}{dx} = -E_D^{\infty}\left(\frac{\langle z^{\infty-2}\rangle^{1/2}}{\lambda_{\infty}^{+}} + \frac{\langle z^{\infty+2}\rangle^{1/2}}{\lambda_{\infty}^{-}}\right) + E_D^{*}\left(\frac{\langle z^{*-2}\rangle^{1/2}}{\lambda_{*}^{+}} + \frac{\langle z^{*+2}\rangle^{1/2}}{\lambda_{*}^{-}}\right); \quad (39)$$

$$U\frac{dL_{\infty}^{\pm}}{dx} + \frac{1}{2}\frac{dU}{dx}L_{\infty}^{\pm} + \frac{1}{4}\frac{dU}{dx}L_D^{\infty} + \frac{1}{4}\langle z^{\infty\pm2}\rangle^{1/2}(L_D^{\infty} - 2L_{\infty}^{\pm})\frac{1}{\rho_s}\frac{d\rho_s}{dx} = 0; \quad (40)$$

$$U\frac{dL_D^{\infty}}{dx} + \frac{1}{2}\frac{dU}{dx}L_D^{\infty} + \frac{1}{2}(L_{\infty}^{+} + L_{\infty}^{-})\frac{dU}{dx} - \frac{1}{4}(L_D^{\infty}(\langle z^{\infty+2}\rangle^{1/2} + \langle z^{\infty-2}\rangle^{1/2}) - 2L_{\infty}^{+}\langle z^{\infty-2}\rangle^{1/2} - 2L_{\infty}^{-}\langle z^{\infty+2}\rangle^{1/2})\frac{1}{\rho_s}\frac{d\rho_s}{dx} = 0. \quad (41)$$

In Equations (38)–(41), the flow profile U (and thus ρ_s, $d\rho_s/dx$, and dU/dx) is now prescribed by the shock transition obtained in Section 4.

The stationary 1D equations for the slab component are given by

$$U\frac{d\langle z^{*\pm2}\rangle}{dx} + \frac{dU}{dx}\left(\left(\frac{1}{2} - b\right)\langle z^{*\pm2}\rangle + \left(3b - \frac{1}{2}\right)E_D^{*}\right) - \frac{1}{2}(\langle z^{*\pm2}\rangle - E_D^{*})\langle z^{\infty\pm2}\rangle^{1/2}\frac{1}{\rho_s}\frac{d\rho_s}{dx} = -2\frac{\langle z^{*\pm2}\rangle\langle z^{\infty\mp2}\rangle^{1/2}}{\lambda_{\infty}^{\pm}} - 2\frac{\langle z^{*\pm2}\rangle\langle z^{*\mp2}\rangle^{1/2}}{\lambda_{*}^{\pm}}; \quad (42)$$

$$U\frac{dE_D^{*}}{dx} + \left(\frac{1}{2} - b\right)E_D^{*}\frac{dU}{dx} + \left(3b - \frac{1}{2}\right) \times E_T^{*}\frac{dU}{dx} - \frac{1}{4}(E_D^{*}(\langle z^{\infty+2}\rangle^{1/2} + \langle z^{\infty-2}\rangle^{1/2}) - \langle z^{*-2}\rangle\langle z^{\infty+2}\rangle^{1/2} - \langle z^{*+2}\rangle\langle z^{\infty-2}\rangle^{1/2})\frac{1}{\rho_s}\frac{d\rho_s}{dx} = -E_D^{*}\left(\frac{\langle z^{\infty-2}\rangle^{1/2}}{\lambda_{\infty}^{+}} + \frac{\langle z^{\infty+2}\rangle^{1/2}}{\lambda_{\infty}^{-}}\right) - E_D^{*}\left(\frac{\langle z^{*-2}\rangle^{1/2}}{\lambda_{*}^{+}} + \frac{\langle z^{*+2}\rangle^{1/2}}{\lambda_{*}^{-}}\right); \quad (43)$$

$$U\frac{dL_{*}^{\pm}}{dx} + \left(\frac{1}{2} - b\right)\frac{dU}{dx}L_{*}^{\pm} + \left(\frac{3}{2}b - \frac{1}{4}\right)\frac{dU}{dx}L_D^{*} - \frac{1}{2}\left(L_{*}^{\pm} - \frac{1}{2}L_D^{*}\right)\langle z^{\infty\pm2}\rangle^{1/2}\frac{1}{\rho_s}\frac{d\rho_s}{dx} = 0; \quad (44)$$

$$U\frac{dL_D^{*}}{dx} - \left(b - \frac{1}{2}\right)\frac{dU}{dx}L_D^{*} + \left(3b - \frac{1}{2}\right) \times (L_{*}^{+} + L_{*}^{-})\frac{dU}{dx} + \frac{1}{2}\left(\left(L_{*}^{-} - \frac{1}{2}L_D^{*}\right)\langle z^{\infty+2}\rangle^{1/2} + \left(L_{*}^{+} - \frac{1}{2}L_D^{*}\right)\langle z^{\infty-2}\rangle^{1/2}\right)\frac{1}{\rho_s}\frac{d\rho_s}{dx} = 0; \quad (45)$$

where $b = 0.22$ is assumed.

In solving the two-component transport Equations (38)–(45), it is convenient to fit a tanh function to the derived HTS structure,

$$U = \frac{1}{2}(U_1 + U_2) - \frac{1}{2}(U_1 - U_2)\tanh\left(\frac{x - x_0}{D_{\rm sh}}\right), \quad (46)$$

where U_1 and U_2 are the upstream and downstream velocities, x_0 is the shock position, and $D_{\rm sh}$ is a shock thickness parameter for the tanh fitting. For reference, we illustrate the derived tanh form of the HTS transition (solid line) and overplot the solution derived in Section 4 (open circles) in Figure 6, where we have assumed $D_{\rm sh} = 10^5$ km and shock compression ratio $r = 2.73$. The turbulence parameters used as upstream values at 84 au are tabulated in Table 4.

Plotted in the top two panels of Figure 7 is the change in the energy density of the forward and backward Elsässer variables across the perpendicular HTS. The majority 2D component experiences a nearly factor of 2 increase across the perpendicular HTS, which is significantly larger than that experienced by the minority slab component. This increase is reflected in the approximately factor of 3 increase in the majority 2D fluctuating magnetic field variance, which is somewhat larger than that of the minority slab magnetic field variance. Similarly, the kinetic energy (velocity variance) in the majority 2D fluctuating velocity component experiences a large increase ($\sim$2.9) compared to the slab component, which is relatively unchanged across the shock. These results are intriguing in that they suggest a large enhancement in the majority 2D component across the perpendicular HTS, which might be consistent with the possibility of additional particle acceleration downstream of the HTS via reconnection-related processes associated with quasi-2D turbulence (Zank et al. 2015).

The normalized residual energy σ_D is plotted in Figure 8. The plot shows that the majority 2D component transitions from an upstream state of near equilibration ($\sigma_D \simeq -0.04$, i.e., magnetic and kinetic energy are approximately equal) to a downstream state that is kinetically dominated ($\sigma_D \simeq 0.45$). A similar but smaller change in the residual energy of the slab component occurs across the perpendicular HTS. The cross-helicity, as shown in Figure 8, is essentially unchanged across the HTS.

The correlation length functions are changed very little across the HTS, as illustrated in Figure 9. By contrast, because of the change in the energy density of the Elsässer variables, the corresponding correlation lengths do change across the shock.

The change in the character of the supersonic solar wind turbulence across the shock is interesting. Burlaga et al. (2006) have suggested, based on *Voyager* 1 magnetic field observations, that a fundamental change in the nature of the interplanetary turbulence occurs across the HTS. They found that the distribution of magnetic fluctuations was essentially

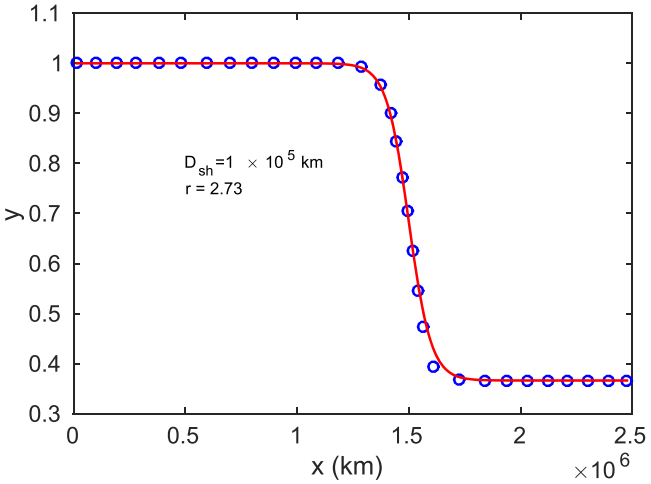

Figure 6. HTS structure derived in Section 4 (blue circles) is fitted by a tanh function given by Equation (46) (red curve). The tanh form of the shock profile is used to evaluate the transmission and generation of quasi-2D and slab turbulence across the HTS.

Table 4
Boundary Values at 84 au Obtained from the Turbulence Transport Model of Section 3

2D Core Model Equations		Slab Model Equations	
$\langle z^{\infty +2}\rangle$	49.79 km^2 s^{-2}	$\langle z^{*+2}\rangle$	14.25 km^2 s^{-2}
$\langle z^{\infty -2}\rangle$	48.41 km^2 s^{-2}	$\langle z^{*-2}\rangle$	14.04 km^2 s^{-2}
E_D^{∞}	-1.73 km^2 s^{-2}	E_D^{*}	-0.06 km^2 s^{-2}
L_{∞}^{+}	7.09×10^8 km^3 s^{-2}	L_{*}^{+}	4.84×10^7 km^3 s^{-2}
L_{∞}^{-}	6.79×10^8 km^3 s^{-2}	L_{*}^{-}	3.91×10^7 km^3 s^{-2}
L_D^{∞}	-1.39×10^9 km^3 s^{-2}	L_D^{*}	-7.24×10^7 km^3 s^{-2}

Note. These values correspond to the turbulent state upstream of the HTS.

Gaussian downstream of the HTS, unlike the lognormal distribution characteristic of the supersonic solar wind, that it was almost isotropic, and had a significant compressible component. By contrast, Burlaga et al. (2009) found that magnetic field fluctuations observed by *Voyager* 2 downstream of the HTS are different than those observed by *Voyager* 1 in possessing instead a downstream lognormal distribution. Nonetheless, Burlaga & Ness (2009) report that the downstream turbulence observed by *Voyager* 2 is also highly compressive. Currently, it is not therefore understood on the basis of *Voyager* 1 and 2 observations how turbulence in the supersonic solar wind is changed on its transition through the perpendicular HTS. Since a shock generates typically high levels of compressible (magnetosonic) fluctuations downstream of a shock (McKenzie & Westphal 1968; Zank et al. 2017), the approach presented above neglects this important component. Nonetheless, even in the context of an NI MHD turbulence transport model, the increase in σ_D from upstream to downstream indicates a greater increase in the downstream kinetic energy density relative to the magnetic field energy density. The upstream turbulence is not however isotropized as it is transmitted through the HTS—instead, the majority quasi-2D component becomes even more dominant downstream. It is possible that the isotropization may rather be the result of the generation of downstream magnetosonic modes by the HTS, which, when superimposed with the NI quasi-2D majority component yields an overall quasi-isotropic distribution in the magnetic field vector components. However, why *Voyager* 1 and *Voyager* 2 should observe quite different downstream turbulent states is quite unclear.

6. Conclusions

There is a close coupling of PUIs, thermal solar wind plasma, and the evolution of low-frequency turbulence throughout the solar wind. PUIs and thermal plasma are not equilibrated in the supersonic solar wind and must therefore be treated as separate and distinct components. Furthermore, PUIs form a nearly isotropic distribution and so contribute both a collisionless heat flux and viscosity to the full plasma system. Both can safely be neglected when evaluating the large-scale solar wind flow, but both are of importance in determining small-scale structures in the solar wind, such as the HTS. We develop a very general theoretical model that incorporates PUIs, solar wind thermal plasma, the interplanetary magnetic field, and low-frequency turbulence to describe the evolution of the large-scale solar wind, PUIs, and turbulence from 1–84 au, the structure of the perpendicular HTS, and the transmission of turbulence into the inner heliosheath. The theoretical model results are compared directly to corresponding quantities derived from *Voyager* 2 and NH SWAP data.

Our principle conclusions can be summarized as follows.

1. We have coupled a non-equilibrated thermal plasma-PUI solar wind model to a model that describes the transport and evolution of low-frequency turbulence throughout the solar wind. Sources of turbulence include stream-shear interactions and the PIU process in the distant heliosphere. The turbulence model is based on the NI MHD description of a majority quasi-2D and minority slab component. The dissipation of turbulence results in the heating of the thermal solar wind plasma.
2. The theoretical model is constrained simultaneously by both *Voyager* 2 thermal plasma and magnetic field observations from 1–75 au and NH SWAP thermal plasma and PUI data between ∼11.26 and 38 au. For both data sets, the theoretical thermal solar wind number density and PUI number density solutions are in excellent agreement. Despite large solar cycle variations in the radial velocity, the theoretical steady-state model solutions are consistent with both sets of observations. Particularly striking is the agreement between theory and observations in the thermal solar wind and PUI pressure and temperature profiles. The *Voyager* 2 pressure and temperature profiles exhibit a flattening and increase, respectively, between ∼20 and 30 au, extending to beyond 75 au. This feature is very well captured by the theoretical model and is a direct consequence of the dissipative heating of the thermal solar wind plasma by the turbulence generated by PUIs in the distant heliosphere. The theoretical solutions match the SWAP observations well, and in particular the PUI pressure and temperature solutions demonstrate an excellent match to the SWAP PUI measurements. However, we note that the PUI temperature is increasing slightly, although it is too soon to conclude that this trend is persistent. If the PUI temperature increase continues with increasing heliocentric distance, we have suggested three possible explanations. The first is that turbulent dissipation may be responsible despite the PUIs being a

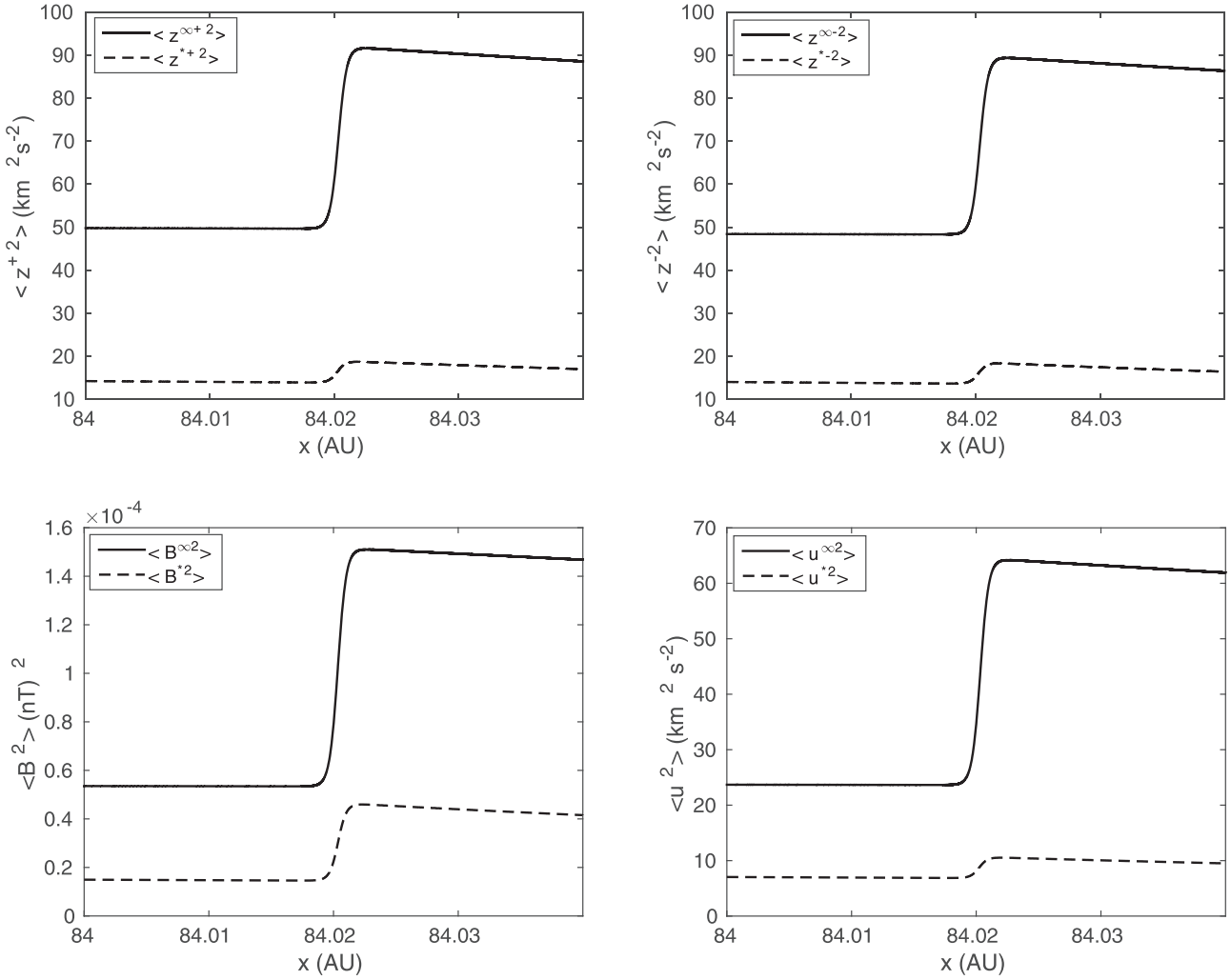

Figure 7. Turbulence intensities across the HTS, located at 84.02 au.

hot, non-equilibrated population, the second may be PUI energization due to second-order Fermi acceleration, and the third may be due to the preferential heating of PUIs by interplanetary shocks.

3. As noted above, the agreement between the theoretical predictions and the PUI observations made by the SWAP instrument are very good. The model uses ionization rate, charge-exchange cross-section, and hydrogen ionization cavity values that are physically acceptable. McComas et al. (2017) used the Vasyliunas & Siscoe (1976) solution to fit the SWAP PUI data, finding quite good agreement although for a large range of β_0 parameter values. Some were thought to be unphysically large (see in particular Figures 10 and 11 in McComas et al. 2017 and the related discussion). In part, the reason for the large values of β_0 may stem from the assumption implicit in the Vasyliunas & Siscoe (1976) model that the neutral H population and the solar wind are cold and that $U_H = 0$, which yields a source term of the form used in Equation (1) of McComas et al. (2017) (see the Appendix for the complete form of the transport equation in the supersonic solar wind). In our formulation, as with that of Holzer (1972) and Isenberg (1986), the solar wind is not assumed to be cold, ensuring that the charge-exchange terms source terms (11)–(13) are included separately from the photoionization source term. With this approach, the theoretical model reproduces the observations well. For more details, see the Appendix.
4. For completeness, we compare in some detail the turbulence transport model predictions with the derived *Voyager* 2 observations. Unlike the Adhikari et al. (2017) results, our results here are more complete in that we compute the fully coupled feedback of PUIs, solar wind thermal plasma heating, and turbulence evolution to determine the background solar wind flow and density necessary to solve the turbulence transport equations. In Adhikari et al. (2017), we simply assumed a specified constant solar wind speed. In this regard, the turbulence transport results presented here are more complete. We find that the theory and observations are consistent, and for more accurately measured quantities such as the magnetic field variance, the agreement is quite striking. Despite the use of a fully coupled model, the turbulence transport results are nonetheless very similar to those presented by Adhikari et al. (2017), and so we do not repeat that discussion here.
5. The corresponding "kinetic energy" related turbulence variables, i.e., the variance in the velocity and density fluctuations $\langle u^2 \rangle$ and $\langle \rho^{\propto 2} \rangle$, can be compared to both *Voyager* 2 and NH SWAP data sets. Despite the greater

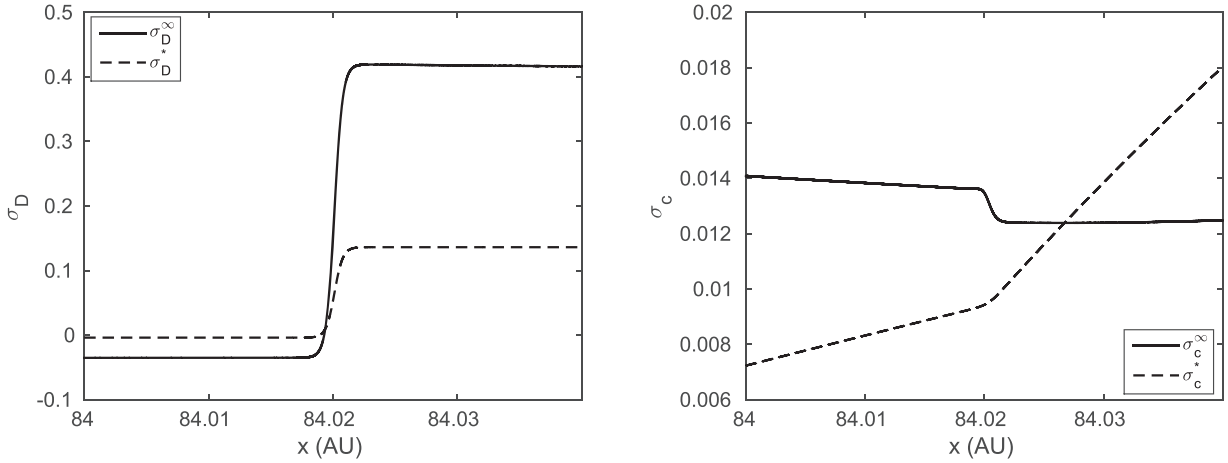

Figure 8. Turbulence intensities across the HTS, located at 84.02 au. The downstream decay of turbulence is due to our assuming no driving or further excitation of turbulence behind the HTS, ensuring that the turbulence dissipates only and further heats the background plasma flow.

difficulty in deriving the velocity and density variances, reasonable to quite good agreement is found between theory and *Voyager* 2 observations, but the model tends to overestimate $\langle u^2 \rangle$ and underestimate $\langle \rho_s^2 \rangle$ compared to the SWAP data, although not very significantly. We speculate that this may be a consequence of the SWAP measurements being made during a during a weaker solar cycle quite unlike prior solar cycles.

6. We use the theoretical model to extrapolate the plasma, PUI, and turbulence solutions to 84 au, the distance at which *Voyager* 2 crossed the perpendicular HTS. By incorporating the collisionless PUI heat flux and viscosity, we determine the structure of the HTS. We find that the shock thickness is $\sim 3.5 \times 10^5$ km and that the shock compression ratio is ~ 2.73. The downstream shock pressure is dominated completely by the PUI component, being heated to $\sim 3.47 \times 10^7$ K across the shock, whereas the thermal solar wind remains relatively cold downstream with a temperature of $\sim 1.55 \times 10^5$ K. These results are similar to those presented by Mostafavi et al. (2017b), although the transverse magnetic field is now included. The shock structure and parameters derived here are consistent with the parameters observed by *Voyager* 2 during the second or TS-2 HTS crossing (Burlaga et al. 2008; Richardson et al. 2008; Richardson 2008).
7. Finally, since PUIs mediate the structure of the HTS, we can use the shock structure model to explore the transmission of NI MHD turbulence across the HTS. Our results show that the majority 2D component is strongly amplified on shock passage compared to the minority slab component. The normalized residual energy increases from ~ -0.04–0.45, i.e., the character of the turbulence changes from a nearly equilibrated distribution in kinetic and magnetic energy density ($\langle u^2 \rangle \sim \langle b^2 \rangle$) to one in which the downstream kinetic energy dominates. The *Voyager* 1 and *Voyager* 2 observations related to the transmission of turbulence across the HTS are somewhat inconclusive, but it would appear that the generation of compressible turbulence at the HTS, which is not included in our approach here, should be incorporated.

This work has been supported in part by the NSF EPSCoR RII-Track-1 Cooperative Agreement OIA-1655280, and *IBEX* subaward SUB 0000167/NASA 80NSSC18k0237. G.P.Z. acknowledges partial support by the NSF/DOE Partnership in Basic Plasma Science and Engineering via NSF grant PHY-1707247 and a NASA award NNX14AJ53G. P.M. acknowledges the support of a NASA Earth and Space Science Fellowship Program grant 16-HELIO16F-0022. E.Z. acknowledges partial support from NASA grant NNX16AG83G. This work was also carried out with partial support from the *IBEX* mission, which is part of NASA's Explorer Program. D.M. acknowledges support from the SWAP instrument effort on the NH mission, which is part of NASA's New Frontiers Program.

Appendix

We provide an outline for the derivation of the model used in the body of this work. This allows us to address to the question of the use of the Vasyliunas & Siscoe (1976) solution in fitting the PUI data observed by NH SWAP. As discussed, the predicted PUI-mediated solar wind model solutions used here fit the SWAP data very well, with the exception of the upturn in PUI temperature at $\sim$35 au, using acceptable physical values for the photoionization and charge-exchange rates. The Vasyliunas & Siscoe (1976) solution used by McComas et al. (2017) matches the SWAP observations for a range of β_0 parameter values, some of which may be unphysically large. The Vasyliunas & Siscoe (1976) solution is derived under the assumption that both the neutral H and solar wind protons are cold, i.e., $T_H = 0 = T_s$, which allows the photoionization and charge-exchange source terms to be combined.

The effect of different choices of β_0 is illustrated in Figure 10. Shown in Figure 10 is a comparison of the data and four models from 10–40 au. The black dots are observations from the NH SWAP instrument. The purple triangles are 2 au averaged results. Red lines and blue lines represent moments of the Vasyliunas & Siscoe (1976) solution with different choices of the rate β_0: the red lines use $\beta_0 = 1.5 \times 10^{-7} s^{-1}$, and blue lines $\beta_0 = 5.63 \times 10^{-7} s^{-1}$ (McComas et al. 2017). The lower value of β_0 is a realistic photoionization value, see, e.g., Bzowski et al. (2013) and the higher value combines both photoionization and charge exchange. The green and cyan lines are results from our PUI

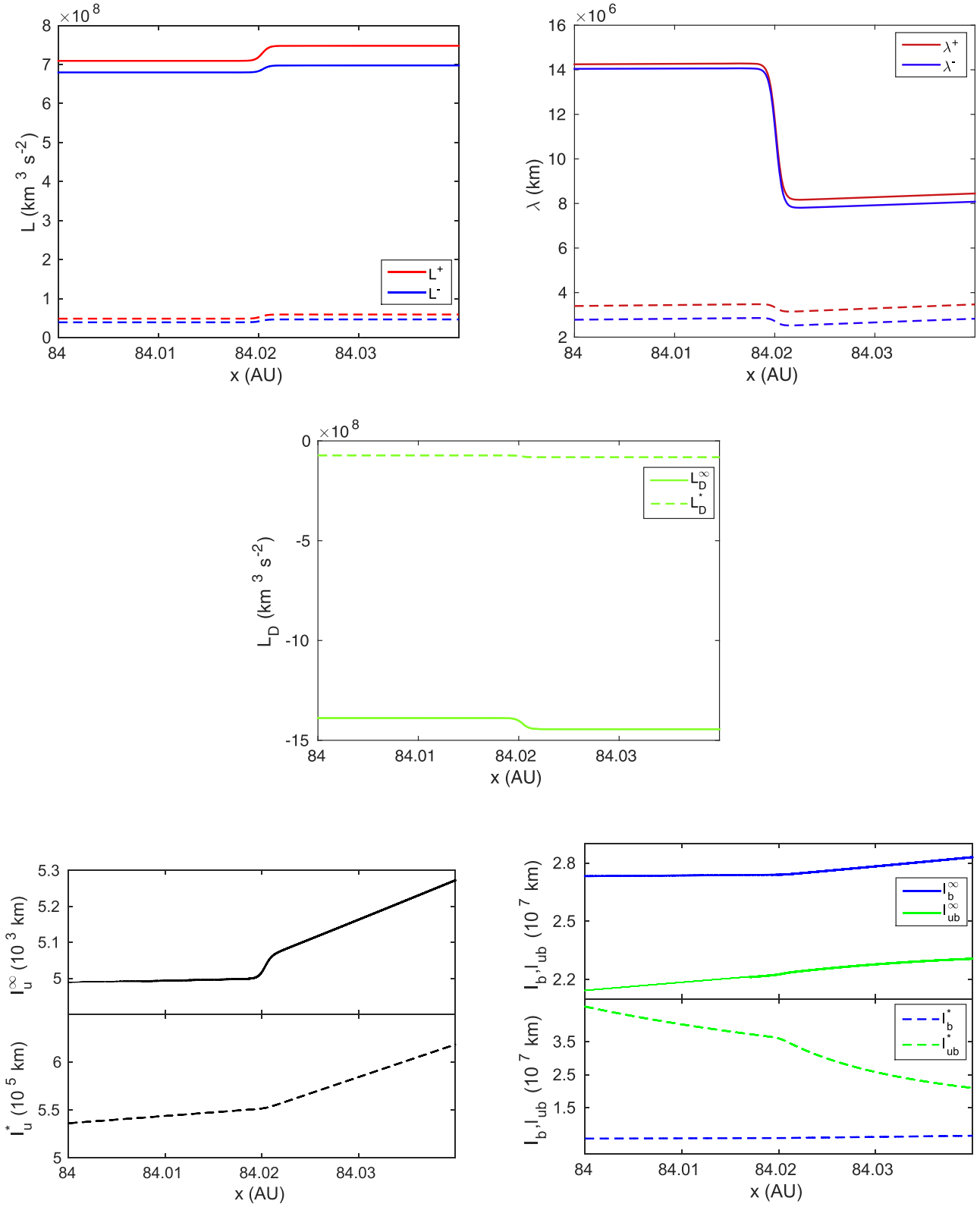

Figure 9. Correlation functions and the correlation lengths across the shock.

continuum, Equations (14)–(20). The green lines correspond to setting the charge-exchange terms between the solar wind protons and interstellar neutral H to zero.

In the first panel, the green line and red line overlay one another. In the third panel, the red and blue lines are overlayed. Evidently, our full continuum solutions are very close to the Vasyliunas & Siscoe (1976) results presented by McComas et al. (2017) when the larger value of β_0 (light blue and dark blue lines, respectively) is used. When the the charge-exchange source terms S_c^s terms are set to zero, the continuum solution is very close to the Vasyliunas & Siscoe (1976) results for smaller β_0 values (green and red lines, respectively). The inclusion of

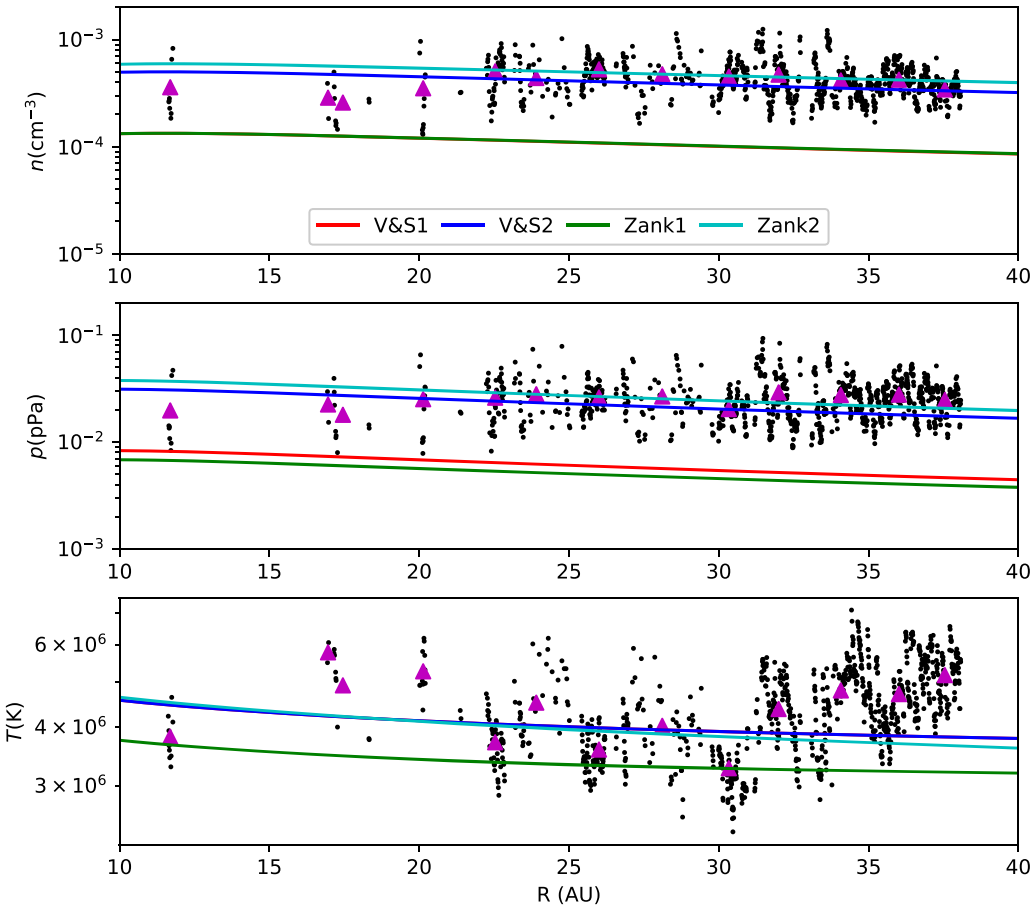

Figure 10. PUI density (top panel), pressure (middle panel), and temperature (bottom panel) derived from different models. Black dots represent the measurements from New Horizon. Magenta triangles represent the 2 au averaged observation. Red and blue lines represent moments of the Vasyliunas & Siscoe (1976) solution with different photoionization rates β_0: red lines use $\beta_0 = 1.5 \times 10^{-7} s^{-1}$, and blue lines use $\beta_0 = 5.63 \times 10^{-7} s^{-1}$ (McComas et al. 2017). Green and cyan lines show the results from Equations (14)–(20). For the green lines, charge exchange between thermal proton and interstellar neutral H (S_c^s) is set to zero.

the additional charge-exchange S_c^s term has a similar effect as increasing the rate β_0.

To illustrate the derivation of the model (1)–(13) from a kinetic perspective and to explicate the origin of the charge-exchange source term, consider pickup protons only. The origin of pickup protons in the supersonic solar wind is both solar wind protons, S^+ say, and pre-existing pickup protons, P^+ say, that experience charge exchange with interstellar neutral H drifting through the heliosphere, shown schematically as

$$S^+ + H \rightarrow P^+ + H; \quad P^+ + H \rightleftarrows H + P^+. \tag{47}$$

Boltzmann's equation for the pickup proton distribution $f_p(\boldsymbol{x}, \boldsymbol{v}, t)$ is

$$\frac{\partial f_p}{\partial t} + \boldsymbol{v} \cdot \nabla f_p + \frac{\boldsymbol{F}}{m} \cdot \nabla_v f_p = \left.\frac{\delta f_p}{\delta t}\right)_{ce} + S_p^{ph} + \left.\frac{\delta f_p}{\delta t}\right)_{wp}, \tag{48}$$

where the collisional term with subscript *ce* corresponding to the charge-exchange process (47) is expressed as (see also Holzer & Banks 1969 and Khabibrakhmanov et al. 1996 for related expressions)

$$\left.\frac{\delta f_p}{\delta t}\right)_{ce}(\boldsymbol{v}) = \int \sigma|\boldsymbol{v} - \boldsymbol{v}'| f_{\mathrm{H}}(\boldsymbol{v}) f_s(\boldsymbol{v}') d\boldsymbol{v}' + \int \sigma|\boldsymbol{v} - \boldsymbol{v}'| f_{\mathrm{H}}(\boldsymbol{v}) f_p(\boldsymbol{v}') d\boldsymbol{v}' - \int \sigma|\boldsymbol{v} - \boldsymbol{v}'| f_p(\boldsymbol{v}) f_{\mathrm{H}}(\boldsymbol{v}') d\boldsymbol{v}'. \tag{49}$$

Here, the distribution functions $f_s(\boldsymbol{x}, \boldsymbol{v}, t)$, $f_{\mathrm{H}}(\boldsymbol{x}, \boldsymbol{v}, t)$, and $f_p(\boldsymbol{x}, \boldsymbol{v}, t)$ refer to solar wind protons, neutral H, and pickup protons, $\boldsymbol{v}$ is the particle velocity, F the force acting on the particles, m the proton (and H) mass, and σ the collisional cross-section. As before, S_p^{ph} is the photoionization source term. The other "collisional" term with subscript *wp* refers to PUI scattering by magnetic turbulence and/or waves.

On assuming that the source and loss terms of charge exchange between pickup protons and H are approximately balanced and that σ is independent of the proton and neutral H velocities, Equation (49) simplifies to

$$\left.\frac{\delta f_p}{\delta t}\right)_{ce}(\boldsymbol{v}) \simeq \int \sigma|\boldsymbol{v} - \boldsymbol{v}'| f_{\mathrm{H}}(\boldsymbol{v}) f_s(\boldsymbol{v}') d\boldsymbol{v}'. \tag{50}$$

If we assume that the solar wind distribution function $f_s(\boldsymbol{x}, \boldsymbol{v}, t)$ is Maxwellian, i.e.,

$$f_s(\boldsymbol{x}, \boldsymbol{v}, t) = \frac{n_s}{(\pi v_{Ts}^2)^{3/2}} e^{-(\boldsymbol{v}-\boldsymbol{U})^2/v_{Ts}^2},$$

$v_{Ts} = \sqrt{3kT_s/m}$ the thermal velocity, then (Pauls et al. 1995)

$$\int |\boldsymbol{v} - \boldsymbol{v}'| f_s(\boldsymbol{v}') d\boldsymbol{v}' = n_s v_{Ts} \left[\frac{e^{-\xi^2}}{\sqrt{\pi}} + \left(\xi + \frac{1}{2\xi} \right) \Phi(\xi) \right]$$
$$\simeq n_s v_{Ts} \sqrt{4/\pi + \xi^2};$$
$$\xi^2 \equiv |\boldsymbol{U} - \boldsymbol{v}|^2 / v_{Ts}^2, \quad (51)$$

and Φ is the error function. Hence, the Boltzmann Equation (48) reduces to

$$\frac{\partial f_p}{\partial t} + \boldsymbol{v} \cdot \nabla f_p + \frac{\boldsymbol{F}}{m} \cdot \nabla_v f_p = \sigma n_s \times \sqrt{\frac{4}{\pi} v_{Ts}^2 + |\boldsymbol{U} - \boldsymbol{U}_{\rm H}|^2} f_{\rm H}(\boldsymbol{v}) + S_p^{ph} + \left. \frac{\delta f_p}{\delta t} \right)_{wp}, \quad (52)$$

where we have assumed that the neutral H velocity in the square root term can be approximated adequately by $\boldsymbol{U}_{\rm H}$.

On returning to the question of the Vasyliunas & Siscoe (1976) solution, if we assume (i) a cold neutral H distribution, (ii) a neutral H drift speed $U_{\rm H} = 0$, and (iii) a cold solar wind plasma, i.e., $T_s = 0$, the charge-exchange source term for the PUIs becomes

$$S_{ch}(r, v) = \sigma n_s U N(r) \frac{\delta(v - U)}{4\pi v^2}. \quad (53)$$

On neglecting S_{ph}, assuming that it is small compared to S_{ch}, Equation (52) is then equivalent to Equation (1) of McComas et al. (2017) with an undefined β_0 parameter. McComas et al. (2017) assume that $\beta_0 \propto r^{-2}$ or $\beta_0 = \sigma n_s U$.

By taking moments of Equation (52), one obtains the corresponding fluid equations for the pickup protons, such as, e.g., the continuity Equation (2). However, taking moments of Equation (52) also introduces the problem of closure related to the higher-order moments such as the pressure tensor and heat flux terms. Since PUIs experience scattering in pre-existing and self-generated turbulence, described by $\delta f_p/\delta t)_{wp}$, the distribution function tends to relax toward isotropy. The simplest form of the pitch-angle scattering operator is the Lorentz operator,

$$\left. \frac{\delta f_p}{\delta t} \right)_{wp} = \frac{\partial}{\partial \mu} \left(\frac{1 - \mu^2}{\tau_s} \frac{\partial f_p}{\partial \mu} \right), \quad (54)$$

where τ_s denotes the turbulence/wave-particle scattering timescale. Zank et al. (2014, 2016) and Zank (2016) use the pitch-angle scattering operator (54) to solve for the distribution function $f_p(\boldsymbol{x}, \boldsymbol{v}, t)$ in terms of an isotropic leading-order term f_{p0}, plus first- and second-order corrections f_{p1} and f_{p2}. This expansion of the pickup proton distribution function yields a Chapman–Enskog closure of the pressure tensor and heat flux PUI terms, which introduces a first-order heat flux and a second-order viscosity. This approach is presented in detail in Zank et al. (2014, 2016) and Zank (2016), and yields Equations (4)–(8).

ORCID iDs

G. P. Zank https://orcid.org/0000-0002-4642-6192
L. Adhikari https://orcid.org/0000-0003-1549-5256
L.-L. Zhao https://orcid.org/0000-0002-4299-0490
P. Mostafavi https://orcid.org/0000-0002-3808-3580
E. J. Zirnstein https://orcid.org/0000-0001-7240-0618
D. J. McComas https://orcid.org/0000-0002-9745-3502

References

Adhikari, L., Zank, G. P., Bruno, R., et al. 2015, ApJ, 805, 63
Adhikari, L., Zank, G. P., Hu, Q., & Dosch, A. 2014, ApJ, 793, 52
Adhikari, L., Zank, G. P., Hunana, P., et al. 2017, ApJ, 841, 85
Adhikari, L., Zank, G. P., Hunana, P., & Hu, Q. 2016a, J Phys.: Conf. Ser., 767, 012001
Adhikari, L., Zank, G. P., Hunana, P., & Hu, Q. 2016b, ApJ, 833, 218
Aggarwal, P., Taylor, D. K., Smith, C. W., et al. 2016, ApJ, 822, 94
Bogdan, T. J., Lee, M. A., & Schneider, P. 1991, JGR, 96, 161
Breech, B., Matthaeus, W. H., Minnie, J., et al. 2008, JGR, 113, 8105
Burlaga, L. F., & Ness, N. F. 2009, ApJ, 703, 311
Burlaga, L. F., Ness, N. F., & Acuña, M. H. 2006, ApJ, 642, 584
Burlaga, L. F., Ness, N. F., Acuña, M. H., et al. 2008, Natur, 454, 75
Burlaga, L. F., Ness, N. F., Acuña, M. H., et al. 2009, ApJ, 692, 1125
Burrows, R. H., Zank, G. P., Webb, G. M., Burlaga, L. F., & Ness, N. F. 2010, ApJ, 715, 1109
Bzowski, M., Sokół, J. M., Tokumaru, M., et al. 2013, in Solar Parameters for Modeling the Interplanetary Background, ed. E. Quémerais, M. Snow, & R.-M. Bonnet (Berlin: Springer), 67
Cannon, B. E., Smith, C. W., Isenberg, P. A., et al. 2014a, ApJ, 787, 133
Cannon, B. E., Smith, C. W., Isenberg, P. A., et al. 2014b, ApJ, 784, 150
Chhiber, R., Subedi, P., Usmanov, A. V., et al. 2017, ApJS, 230, 21
Engelbrecht, N. E. 2017, ApJL, 849, L15
Engelbrecht, N. E., & Burger, R. A. 2013, ApJ, 772, 46
Fisher, M. K., Argall, M. R., Joyce, C. J., et al. 2016, ApJ, 830, 47
Florinski, V., Zank, G. P., & Pogorelov, N. V. 2003, JGR, 108, 1228
Gloeckler, G., & Geiss, J. 1998, SSRv, 86, 127
Gloeckler, G., Schwadron, N. A., Fisk, L. A., & Geiss, J. 1995, GeoRL, 22, 2665
Gloeckler, G., Geiss, J., Balsiger, H., et al. 1992, A&AS, 92, 267
Hollick, S. J., Smith, C. W., Pine, Z. B., et al. 2018a, ApJ, 863, 75
Hollick, S. J., Smith, C. W., Pine, Z. B., et al. 2018b, ApJ, 863, 76
Holzer, T. E. 1972, JGR, 77, 5407
Holzer, T. E., & Banks, P. M. 1969, P&SS, 17, 1074
Holzer, T. E., & Leer, E. 1973, Ap&SS, 24, 335
Hossain, M., Gray, P. C., Pontius, D. H., Jr., Matthaeus, W. H., & Oughton, S. 1995, PhFl, 7, 2886
Hunana, P., & Zank, G. P. 2010, ApJ, 718, 148
Isenberg, P. A. 1986, JGR, 91, 9965
Isenberg, P. A., Chih, P. P., & Fisk, L. A. 1985, JGR, 90, 12
Isenberg, P. A., Smith, C. W., Matthaeus, W. H., & Richardson, J. D. 2010, ApJ, 719, 716
Khabibrakhmanov, I. K., Summers, D., Zank, G. P., & Pauls, H. L. 1996, ApJ, 469, 921
Kryukov, I. A., Pogorelov, N. V., Zank, G. P., & Borovikov, S. N. 2012, in AIP Conf. Ser. 1436, Physics of the Heliosphere, ed. J. Heerikhuisen et al. (Melville, NY: AIP), 48
Le Roux, J. A., & Ptuskin, V. S. 1998, JGR, 103, 4799
Lee, M. A., & Ip, W.-H. 1987, JGR, 92, 11041
Lockwood, M., Owens, M. J., Barnard, L., Davis, C. J., & Steinhilber, F. 2011, GeoRL, 38, L22105
Matthaeus, W. H., Bieber, J. W., & Zank, G. P. 1995, RvGeo, 33, 609
Matthaeus, W. H., Zank, G. P., Smith, C. W., & Oughton, S. 1999, PhRvL, 82, 3444
McComas, D., Allegrini, F., Bagenal, F., et al. 2008, SSRv, 140, 261
McComas, D. J., Zirnstein, E. J., Bzowski, M., et al. 2017, ApJS, 233, 8
McKenzie, J. F., & Westphal, K. O. 1968, PhFl, 11, 2350
Mostafavi, P., & Zank, G. P. 2018, ApJL, 854, L15
Mostafavi, P., Zank, G. P., & Webb, G. M. 2017a, J Phys.: Conf. Ser., 900, 012016
Mostafavi, P., Zank, G. P., & Webb, G. M. 2017b, ApJ, 841, 4
Oughton, S., Matthaeus, W. H., Smith, C. W., Breech, B., & Isenberg, P. A. 2011, JGRA, 116, 8105
Palmer, I. D. 1982, RvGSP, 20, 335
Pauls, H. L., Zank, G. P., & Williams, L. L. 1995, JGR, 100, 21595

Randol, B. M., Elliott, H. A., Gosling, J. T., McComas, D. J., & Schwadron, N. A. 2012, ApJ, 755, 75
Randol, B. M., McComas, D. J., & Schwadron, N. A. 2013, ApJ, 768, 120
Reames, D. V. 1999, SSRv, 90, 413
Richardson, J. D. 2008, GeoRL, 35, 23104
Richardson, J. D., Kasper, J. C., Wang, C., Belcher, J. W., & Lazarus, A. J. 2008, Natur, 454, 63
Richardson, J. D., Wang, C., & Burlaga, L. F. 2004, AdSpR, 34, 150
Shebalin, J. V., Matthaeus, W. H., & Montgomery, D. 1983, JPlPh, 29, 525
Shiota, D., Zank, G. P., Adhikari, L., et al. 2017, ApJ, 837, 75
Smith, C. W., Aggarwal, P., Argall, M. R., et al. 2017, J Phys.: Conf. Ser., 900, 012018
Smith, C. W., Matthaeus, W. H., Zank, G. P., et al. 2001, JGR, 106, 8253
Usmanov, A. V., Goldstein, M. L., & Matthaeus, W. H. 2014, ApJ, 788, 43
Usmanov, A. V., Matthaeus, W. H., Breech, B. A., & Goldstein, M. L. 2011, ApJ, 727, 84
Vasyliunas, V. M., & Siscoe, G. L. 1976, JGR, 81, 1247
Verdini, A., Velli, M., Matthaeus, W. H., Oughton, S., & Dmitruk, P. 2010, ApJL, 708, L116
Wallis, M. 1971, NPhS, 233, 23
Wiengarten, T., Oughton, S., Engelbrecht, N. E., et al. 2016, ApJ, 833, 17
Williams, L. L., & Zank, G. P. 1994, JGR, 99, 19229
Williams, L. L., Zank, G. P., & Matthaeus, W. H. 1995, JGR, 100, 17059
Zank, G. P. 1999, SSRv, 89, 413
Zank, G. P. 2015, ARA&A, 53, 449
Zank, G. P. 2016, GSL, 3, 22
Zank, G. P., Adhikari, L., Hunana, P., et al. 2017, ApJ, 835, 147
Zank, G. P., Adhikari, L., Hunana, P., et al. 2018, ApJ, 854, 32
Zank, G. P., Dosch, A., Hunana, P., et al. 2012a, ApJ, 745, 35
Zank, G. P., Du, S., & Hunana, P. 2017, ApJ, 842, 114
Zank, G. P., Heerikhuisen, J., Pogorelov, N. V., Burrows, R., & McComas, D. 2010, ApJ, 708, 1092
Zank, G. P., Hunana, P., Mostafavi, P., & Goldstein, M. L. 2014, ApJ, 797, 87
Zank, G. P., Hunana, P., Mostafavi, P., et al. 2015, ApJ, 814, 137
Zank, G. P., Jetha, N., Hu, Q., & Hunana, P. 2012b, ApJ, 756, 21
Zank, G. P., & Matthaeus, W. H. 1992, JGR, 97, 17189
Zank, G. P., & Matthaeus, W. H. 1993, PhFl, 5, 257
Zank, G. P., Matthaeus, W. H., Bieber, J. W., & Moraal, H. 1998, JGR, 103, 2085
Zank, G. P., Matthaeus, W. H., & Smith, C. W. 1996, JGR, 101, 17093
Zank, G. P., Mostafavi, P., & Hunana, P. 2016, J Phys.: Conf. Ser., 719, 012014
Zank, G. P., Pauls, H. L., Cairns, I. H., & Webb, G. M. 1996, JGR, 101, 457
Zhao, L.-L., Adhikari, L., Zank, G. P., Hu, Q., & Feng, X. S. 2017, ApJ, 849, 88
Zhao, L.-L., Adhikari, L., Zank, G. P., Hu, Q., & Feng, X. S. 2018, ApJ, 856, 94
Zhao, L.-L., Qin, G., Zhang, M., & Heber, B. 2014, JGRA, 119, 1493
Zhao, L.-L., & Zhang, H. 2015, ApJ, 805, 6
Zirnstein, E. J., McComas, D. J., Kumar, R., et al. 2018, PhRvL, 121, 075102